Hydroclimatic trends during 1950–2018 over global land

Aiguo Dai[1]

Abstract

Global hydroclimatic changes from 1950 to 2018 are analyzed using updated data of land precipitation, streamflow, and an improved form of the Palmer Drought Severity Index. The historical changes are then compared with climate model-simulated response to external forcing to determine how much of the recent change is forced response. It is found that precipitation has increased from 1950 to 2018 over mid-high latitude Eurasia, most North America, Southeast South America, and Northwest Australia, while it has decreased over most Africa, eastern Australia, the Mediterranean region, the Middle East, and parts of East Asia, central South America, and the Pacific coasts of Canada. Streamflow records largely confirm these precipitation changes. The wetting trend over Northwest Australia and Southeast South America is most pronounced in austral summer while the drying over Africa and wetting trend over mid-high latitude Eurasia are seen in all seasons. Coupled with the drying caused by rising surface temperatures, these precipitation changes have greatly increased the risk of drought over Africa, southern Europe, East Asia, eastern Australia, Northwest Canada, and southern Brazil. Global land precipitation and continental freshwater discharge show large interannual and inter-decadal variations, with negative anomalies during El Niño and following major volcanic eruptions in 1963, 1982, and 1991; whereas their decadal variations are correlated with the Interdecadal Pacific Oscillation (IPO) with IPO's warm phase associated with low land precipitation and continental discharge. The IPO and Atlantic multidecadal variability also dominate multidecadal variations in land aridity, accounting for 90% of the multidecadal variance. CMIP5 multi-model ensemble mean shows decreased precipitation and runoff and increased risk of drought during 1950–2018 over Southwest North America, Central America, northern and central South America (including the Amazon), southern and West Africa, the Mediterranean region, and Southeast Asia; while the northern mid-high latitudes, Southeast South America, and Northwest Australia see increased precipitation and runoff. The consistent spatial patterns between the observed changes and the model-simulated response suggest that many of the observed drying and wetting trends since 1950 may have resulted at least partly from historical external forcing. However, the drying over Southeast Asia and wetting over Northwest Australia are absent in the 21st century projections.

Keywords Hydroclimate · Trends · Precipitation · Streamflow · Drought · PDSI · CMIP5 · Global land

1 Introduction

Increased CO_2 and other greenhouse gases (GHGs) in the atmosphere will not only raise Earth's surface temperature, but also induce large changes in precipitation, runoff and streamflow, drought and other hydroclimatic fields (Meehl et al. 2007; Scheff and Frierson 2012; Collins et al. 2013; Dai 2013a, 2016; Cook et al. 2014, 2020; Trenberth et al. 2014; Zhao and Dai 2017; Dai et al. 2018), which may cause larger damages to human society and the environment than the concurring warming. Thus, documenting and understanding long-term changes in these hydroclimatic fields are critically important under our changing climate.

Under increasing GHGs, climate models project increased precipitation over most of the globe except for the subtropical subsidence regions (e.g., Meehl et al. 2007; Collins et al. 2013), where enhanced drying from increased vertical gradients of specific humidity and increased subsidence make it hard to form clouds and precipitation in the future warmer climate (Chou et al. 2009; Dai et al. 2018; Huang et al. 2021). Surface runoff and streamflow changes generally follow those of precipitation (Meehl et al. 2007;

✉ Aiguo Dai
   adai@albany.edu

1   Department of Atmospheric and Environmental Sciences, University at Albany, SUNY, Albany, New York 12222, USA

Collins et al. 2013; Zhao and Dai 2015; Dai 2016), although changes in precipitation characteristics (Trenberth et al. 2003; Sun et al. 2007), evapotranspiration (Dong and Dai 2017; Dai et al. 2018) and human activities (Döll et al. 2009; Vicente-Serrano et al. 2019) can induce additional features. Rising air temperatures, coupled with small decreases in near-surface relative humidity (Collins et al. 2013; Vicente-Serrano et al. 2018; Chen et al. 2020), lead to large increases in atmospheric demand for moisture (often measured by potential evapotranspiration PET) over all land areas (Feng and Fu 2013; Scheff and Frierson 2014; Fu and Feng 2014; Fu et al. 2016; Zhao and Dai 2015, 2017). Combined with decreased precipitation over many subtropical regions and a flattening of the histograms of soil moisture, runoff and the Palmer Drought Severity Index (PDSI) (Zhao and Dai 2015), the enhanced PET greatly increases the risk of future drought over most land areas (Burke and Brown 2008; Dai 2011a, 2013a; Cook et al. 2014, 2020; Prudhomme et al. 2014; Zhao and Dai 2015, 2017).

These model-projected long-term changes in response to increased GHGs are, however, often overshadowed by large internal variability, especially at the local and regional scales, making them unapparent in individual realizations (such as the observations or individual model simulations) during the recent and near-future decades (Deser et al. 2012a, b, 2014; Dai and Bloecker 2019). Furthermore, large uncertainties due to instrumental and sampling errors exist in the available datasets for precipitation, runoff and streamflow, PDSI and other hydroclimatic fields (Dai 2016; Dai and Zhao 2017); they make it difficult to reliably quantify historical changes in these fields over the global land (Trenberth et al. 2014). In contrast to the model-projected future changes, the historical changes also include externally-forced response to episodic volcanic eruptions and decadal variations in anthropogenic aerosols, ozone and CFCs (Meinshausen et al. 2011); these forced short-term changes are often merged with other internal variations (Hua et al. 2019; Qin et al. 2020a, b), further complicating the detection and separation of the forced signal in historical data.

Many studies have attempted to quantify historical changes in the mean of land precipitation, streamflow, PDSI and other drought indices, although few of them were able to synthesize/compare these changes or quantify the changes resulting from external forcing and internal variability. For land precipitation, many raingauge-derived datasets go back to around 1900, but raingauge coverage was poor over many regions before the 1950s (Dai et al. 1997; Harris et al. 2014; Schneider et al. 2018; Sun et al. 2018); and these datasets have been used to quantify historical changes in monsoon rainfall (Wang and Ding 2006; Wang et al. 2012; Zhang and Zhou 2011), precipitation over dry and wet regions (Liu and Allen 2013; Huang et al. 2017) and global land (Dai and Zhao 2017). These studies show that precipitation has increased since 1950 over northern and eastern Europe, the central United States, northwestern Australia and southeastern South American, but decreased over most Africa, East and South Asia, southern Europe, and eastern Australia (Dai and Zhao 2017); and some of these changes over the United State, Africa, Australia and South America are associated with the phase change in the Interdecadal Pacific Oscillation (IPO) (Dai 2013b; Dong and Dai 2015), rather than GHG-induced global warming. This appears to be also the case for recent precipitation changes over the tropical Pacific (Gu and Adler 2013). The precipitation change patterns since 1950 are broadly consistent among different datasets and largely confirmed by the basin-mean runoff changes inferred from streamflow records (Dai et al. 2009, 2016). The regional decreases in precipitation and increased PET under rising air temperatures lead to surface drying, as measured by PDSI and SPEI (Vicente-Serrano et al. 2020), since 1950 over most Africa, East and South Asia, southern Europe, high-latitude North America and eastern Australia (Dai et al. 2004; Dai 2011b; Trenberth et al. 2014; Dai and Zhao 2017; Vicente-Serrano et al. 2020), although uncertainties in radiation and surface wind data as well as issues in land precipitation data since the 1990s in some of the widely used datasets could weaken the PDSI trends (van der Schrier et al. 2011, 2013; Sheffield et al. 2012; Dai and Zhao 2017).

As mentioned above, detecting anthropogenic influences in historical precipitation and other related hydroclimatic fields is difficult due to their large internal variability. Nevertheless, precipitation increases in northern mid-high latitudes and decreases in the subtropics in the 20th century (Dai et al. 1997) is attributed partly to human influences (Zhang et al. 2007). On the other hand, many studies attributed a large part of recent changes since the 1950s in regional precipitation over the United States, Africa, Australia and South America, as well as the tropical Pacific rainfall since 1979 (Gu and Adler 2013), to the phase changes in the IPO (Dai 2013a; Dong and Dai 2015) and the Atlantic Multidecadal Oscillation (AMO) (Knight et al. 2006; Hua et al. 2019), although some of the AMO-like multi-decadal variations may be forced by volcanic and anthropogenic aerosols (Qin et al. 2020a). The IPO-induced and other internal variability makes the local and regional precipitation trends since 1979 statistically insignificant over most of the globe up to now and for the near future (Dai and Bloecker 2019). The internal variability also makes the PDSI trends since 1920 differ from the externally-forced response over the United State, West Africa, and other regions, even though the global-mean trend is consistent with the model-simulated change (Dai 2013).

While many previous studies have examined historical changes in a single hydroclimatic field, very few of them have examined them together to make a physically consistent picture about historical hydroclimatic changes over global

land. In this study, I attempt to (1) update the trend analysis up to 2018 for land precipitation, streamflow or runoff and PDSI using available new data; (2) compare, verify and synthesize their trends to present a more complete and convincing picture of the historical hydroclimatic trends; and (3) perform a first-order estimate of the contribution by historical external forcing to the historical trends using CMIP5-model simulated response and a maximum covariance analysis (MCA). Here I focus on the mean changes in various hydroclimate fields, rather than changes in extremes such as drought events. Also, the goal of the comparison with model-simulated changes is to provide a large-scale assessment of whether the observed change patterns are qualitatively consistent with the observations, rather than to provide a quantitative attribution analysis, as done previously (e.g., Marvel et al. 2019; Bonfils et al. 2020). The results should provide an updated and more complete view on historical hydroclimatic trends and on the role of external forcing. This paper will also serve as the reference for our updated streamflow (https://rda.ucar.edu/datasets/ds551.0/) and PDSI (https://rda.ucar.edu/datasets/ds299.0/) datasets that have been widely used by the community.

2 Data and method

We used the updated versions of the gridded monthly precipitation products (on 2.5° grids) from the Global Precipitation Climatology Centre (GPCC v2018 or v8, for 1891–2016; Schneider et al. 2018), the Climate Research Unit (CRU, TS 4.02, for 1901–2017; Harris et al. 2014), a merged precipitation product (referred to as DaiP) using precipitation from Dai et al. (1997) (for years before 1948), Chen et al. (2002) (for 1948–1978), and GPCP v2.3 dataset (for 1979–2018; Adler et al. 2018), and the University of Delaware precipitation data set v5.01 for 1900–2017 (referred to as UDelP, see http://climate.geog.udel.edu/~climate/html_pages/Global2017/README.GlobalTsP2017.html). These are analyzed precipitation products based on raingauge records, except for GPCP data, which also used satellite estimates over sparsely sampled land areas by raingauges. Typically, raingauge coverages are poor over central Africa, the Amazon, the Tibetan Plateau and other sparsely populated areas, especially before about 1950. The coverage also decreases since the 1990s in all these products (Sheffield et al. 2012; Trenberth et al. 2014) partly due to the time delay in the archiving process and loss of manually operated stations. For the period with good raingauge coverage from about 1950–1990, all these products show very similar global land precipitation variations, but they differ substantially for the earlier decades and the most recent years since the middle 1990s (Dai and Zhao 2017). The GPCC product used much more raingauge records and thus is likely to be more reliable than the other

products for the recent years since the 1990s (Dai and Zhao 2017). Thus, we will mainly use the GPCC product for long-term precipitation trend analyses, although the other products were also examined. Since only the GPCP v2.3 product is continuously updated to near real time, we used the GPCP data for the last few years to extend the other products to the end of 2018 (the latest time with data in spring 2019 when I started the analysis) by adding GPCP's anomalies (relative to 1961–1990 mean) to the 1961–1990 mean of the product being extended, so that all the products analyzed here end in December 2018 and are homogeneous. The GPCP used the land data analysis from GPCC and it has similar variations and change for land precipitation to GPCC and the other products for the period since 1979.

To update our continental discharge analysis (Dai and Trenberth 2002; Dai et al. 2009; Dai 2016), I devoted a major effort to obtain and process updated downstream river-flow gauge data from the Global Ruff Data Centre (https://www.bafg.de) for about 220 ocean-reaching rivers around the world, from USGS (https://nwis.waterdata.usgs.gov/nwis) for 71 U.S. rivers, the Water Service of Canada (http://www.ec.gc.ca/rhc-wsc/) for 15 Canadian rivers, and the Brazilian National Water Agency (http://www.snirh.gov.br/hidroweb/publico/apresentacao.jsf) for 131 Brazilian rivers. Together, 261 of the 921 world's largest rivers included in the Dai and Trenberth river discharge dataset (https://rda.ucar.edu/datasets/ds551.0/) were updated to as late as December 2018. For updating our continental discharge estimates of Dai et al. (2009), streamflow data for other 146 rivers were also updated to December 2018 using either basin-mean precipitation data or scPDSIpm that is significantly correlated with historical streamflow records using linear regression following Dai et al. (2009). Annual river flow rates are highly correlated with basin-mean precipitation rates for most of world's major rivers (Dai et al. 2009; Dai 2016), thus the river flow and precipitation data provide us an opportunity to cross check and verify the long-term trends in these physically-related, but independently measured hydroclimatic fields.

Another hydroclimate field examined here is the self-calibrated PDSI with the Penman-Monteith potential evapotranspiration (scPDSIpm), which is a calculated index using monthly precipitation, surface air temperature, and other meteorological data (Dai 2011b). The scPDSIpm is an improved version of the original PDSI devised by Palmer (1965); it is a smoothed measure of near-surface dryness departures estimated using a simple surface water balance model that has been used to quantify drought and aridity changes over the United States and other regions (Dai 2011b; van der Schrier et al. 2011, 2013). The use of the more realistic Penman-Monteith PET requires data for surface net radiation, vapor pressure, surface air pressure and wind speed, whose historical data are less reliable (Dai and

Zhao [2017]). We used the CRU TS4.02 data for surface air temperature, vapor pressure and cloud cover, and other reanalysis data for the other variables, as described in Dai and Zhao ([2017]). Because scPDSIpm used the same precipitation products analyzed here, its changes are not independent of those in precipitation data, although the scPDSIpm also includes the influences from rising surface air temperatures and water vapor deficits. We included the scPDSIpm here as a measure of surface aridity partly because it or its variants have been widely used in the literature. Like all other drought indices, the PDSI has its limitations (Dai [2011a]). However, our previous validation using observed soil moisture, streamflow, and land water storage (Dai et al. [1997], [2004]; Dai [2011b]) and comparisons with model-projected soil moisture and runoff changes (Zhao and Dai [2015]) suggest that it is a reasonable measure of aridity and drought that can help us quantify the drying effect from rising temperatures alone.

Although the precipitation (P), streamflow or runoff (R), and scPDSIpm data are available back to around 1900 over many land areas, our trend analysis will focus on 1950–2018 as data before 1950 are less reliable and have poor global coverage. We also focus on the annual-mean trends, although seasonal differences in P trends are examined. To estimate how much of the observed trends may result from historical GHG and other external forcing, we also analyzed the 1950–2018 trends in P, R, and scPDSIpm from the multi-model ensemble mean (MMM) of the all-forcing historical (up to 2005) and RCP4.5 (for 2006–2018) simulations by the models (40 models for P, 33 models for R and 14 models for scPDSIpm) participated in the phase 5 of the Coupled Model Inter-comparison Project (CMIP5) (Taylor et al. [2012]; https://pcmdi.llnl.gov/mips/cmip5/). We used the CMIP5 data because these model data were used and described in our previous studies (Zhao and Dai [2015], [2017]; Dai [2016]; Dai et al. [2018]) and the number of models with required data from the new CMIP6 archive was small at the time of my analysis. Besides comparing the trend patterns between observations and the CMIP5 MMM, we also performed maximum covariance analyses (MCA, Bretherton et al. [1992]) of the observed and model-simulated precipitation or scPDSIpm fields, with the goal to identify the component in historical P or scPDSIpm whose temporal and spatial patterns are similar to those in the CMIP5 MMM. Since the CMIP5 MMM represents primarily the forced response to GHG and other historical forcing as internal variations are uncorrelated among the individual model simulations and thus are smoothed out during the ensemble averaging, we may consider this component in the historical data as the forced response to historical GHG and other forcing. As the model-simulated historical changes may contain decadal changes forced by historical changes in volcanic and anthropogenic aerosols (Qin et al. [2020a]) that are absent in

the future forcing, we also compare the historical and future change patterns to identify any regional differences.

3 Historical trends from 1950 to 2018

3.1 Historical changes in land precipitation, streamflow and discharge

Figure [1] shows the 1950–2018 trend maps for annual precipitation (from GPCCv8), basin-mean runoff inferred from trends in downstream river flow data, and scPDSIpm. The P trend patterns are similar in the other three datasets with some regional differences (not shown). In general, both the precipitation and streamflow records show wetting trends over the central and eastern US, Alaska, Southeast South America, mid-high latitude Asia, and Northwest Australia, but drying trends over most Africa, southern Europe, the Middle East, northern India, Northeast China, Japan, and eastern Australia (Fig. [1]a, b). However, over northern Europe, precipitation increases in all the P products while the river flow data show mixed signals (Fig. [1]a, b), likely due to insufficient streamflow data over there. Over the Amazon river basin, streamflow data show an insignificant increasing trend while precipitation data show both increases and decreases within the basin (Fig. [1]a, b), which are also seen in the other P products. Overall, the trend patterns from the raingauge and streamflow records are broadly consistent with each other, which provides us some confidence in these trends. The scPDSIpm trend patterns largely follow those of precipitation, with widespread drying over Africa, southern Europe, the Middle East, Southeast Asia, eastern Australia, Northwest Canada, and parts of Brazil; but wetting over the regions with large precipitation increases.

The precipitation increases over mid-high latitude Eurasia occur mainly in the cold season, while the P increase over the US is most widespread during September–October–November (SON) (Fig. [2]). Over western Australia, precipitation increases greatly during austral summer but decreases in its winter, while the drying over eastern Australia is particularly strong during March–April–May (MAM) (Fig. [2]). Over Southeast South America, precipitation increases in all seasons except its winter when it decreases. On the other hand, precipitation over most Africa decreases throughout the year, especially during MAM and SON (Fig. [2]). Thus, precipitation trends during 1950–2018 differ greatly among the seasons over many land regions.

To further examine the precipitation changes for the 16 regions outlined in Fig. [1]a, in Fig. [3] we show their regionally-averaged precipitation anomalies from 1950 to 2018 using the four P datasets, which show similar variations and changes over most of the years for all the regions. Some noticeable differences are seen over Alaska, Northwest
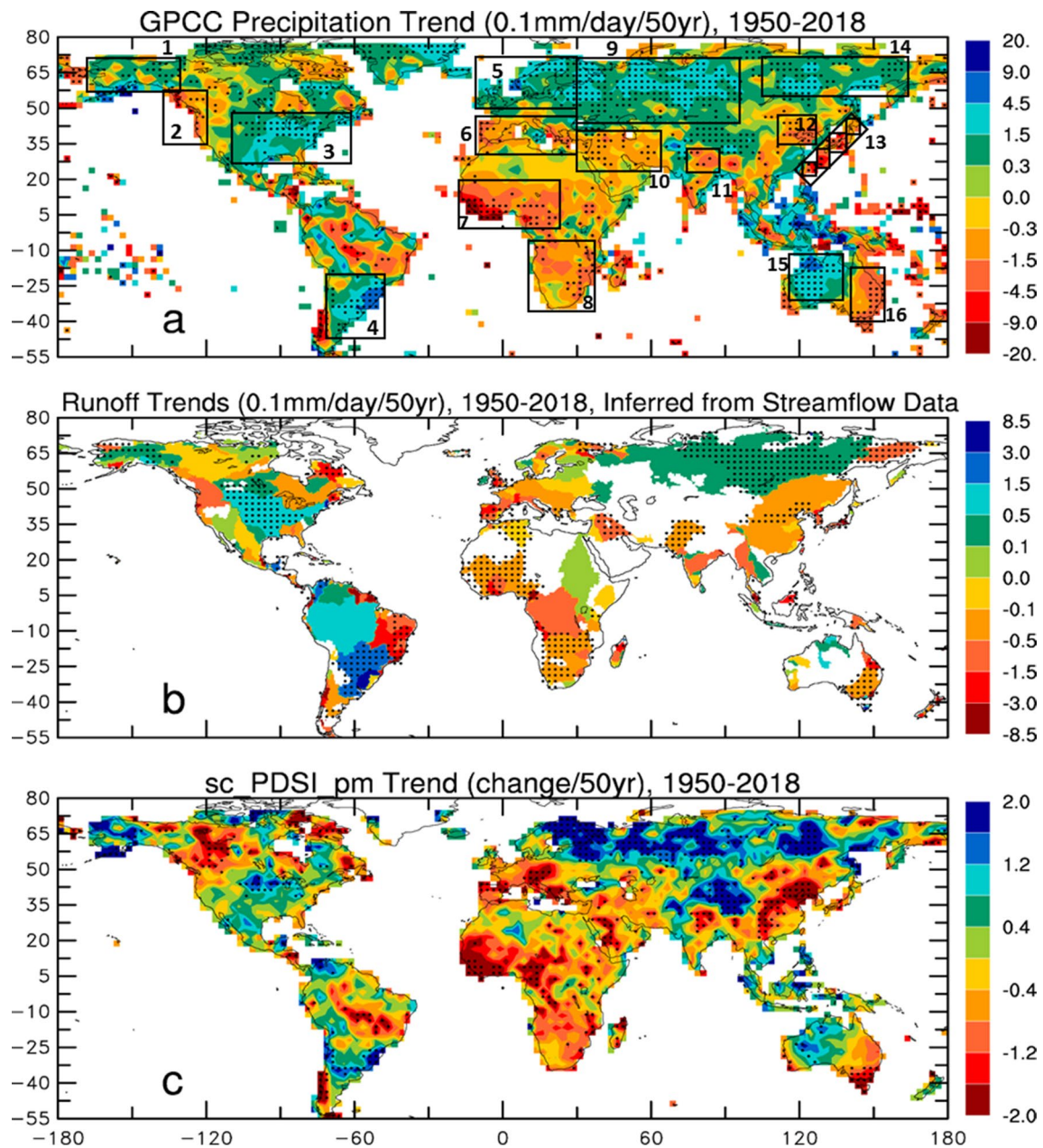
Fig. 1 Linear trends during 1950–2018 in annual **a** precipitation from GPCC v8 (in 0.1mm/day per 50 years), **b** runoff inferred from records of downstream river flow rates (in 0.1mm/day per 50 years), and **c** scPDSIpm. The GPCCv8 dataset, which ends in December 2016, was extended to December 2018 using anomalies from GPCP v2.3 data.

Blank land areas in **b** do not have runoff into the oceans or do not have enough observations. Stippling indicates the trend is statistically significant at the 5% level based on a Student *t* test with the autocorrelation being accounted for. The 16 outlined boxes in **a** represent the 16 regions used in Fig. 3 for regional precipitation

North America (region 2, after 2013), the central-eastern US (after 2005), central Eurasia (before 1977), and Siberia (during the 1960s and 1970s for UDelP) (Fig. 3). Long-term P changes are evident for West and Southern Africa, the Mediterranean, central Eurasia, the Middle East, Siberia, and eastern Australia. In general, large year-to-year fluctuations overshadow the long-term trend, making it less obvious. Some regions (e.g., West Africa and Siberia) show

multi-decadal variations, rather than a monotonic decreasing or increasing trend from 1950 to 2018.

As an example, Fig. 4 shows the time series of the yearly (October–September) river flow rate from the farthest downstream gauge (thick solid line) together with the basin-averaged yearly precipitation rate (dashed line, from GPCCv8) for world's six largest rivers. The two time series are significantly correlated for the six rivers (with the

correlation coefficient $r \approx 0.6–0.8$). Given the large spatial sampling errors in basin-mean precipitation (especially over the Brahmaputra and Amazon) and the variations and changes in evapotranspiration (ET) (Dong and Dai 2017), it is remarkable that the streamflow and precipitation correlation would reach as high as over 0.80 for some of the rivers (e.g., the Orinoco and Changjiang or Yangtze). Such a high consistency between the two independent records suggests that the variations and long-term changes in these data are likely to be real, although some discrepancies exist during certain years, e.g., during 2007–2010 for Amazon, and during 1984–1990 and 1994–1997 for Congo (Fig. 4). To the first order, the basin-mean precipitation appears to be the primary driver of the fluctuations and long-term changes in downstream yearly river flow rates for the world's largest rivers, while human influences (through damning and withdrawal of stream-water) and changes in ET play only a secondary role as noticed previously (Dai et al. 2009).

Streamflow in the Amazon river declined from the late 1940s to around 1970 and then recovered to a stable and normal level with large interannual fluctuations compared with the 1950s and 1960s, and relatively low levels for 2016–2018 (Fig. 4a). In contrast, streamflow in Congo was relatively high from around 1960–1971, thereafter it stayed in relatively low levels until the middle 1990s (Fig. 4b). Streamflow in Orinoco changed little during 1948–2018, with large multi-year fluctuations (e.g., low from 1957 to

Fig. 3 Time series of annual precipitation anomalies (relative to ▶ 1950–2018 mean, in mm/day) from 1950–2018 averaged over the 16 regions outlined in Fig. 1a based on the GPCCv8 (black), DaiP (red), CRU TS4.02 (blue), and University of Delaware (magenta) datasets. The 16 regions include: **a** Alaska (130–167.5° W, 57.5–62.5° N), **b** Northwest North America (120–137.5° W, 35–57.5° N), **c** Central-eastern US (60–110° W, 27.5–47.5° N), **d** Southeast South America (47.5–72.5° W, 20–47.5° S), (e) Northern Europe (10 W–30° E, 50–72.5° N), **f** the Mediterranean region (10° W–30° E, 30–46° N), g West Africa (17.5° W–22.5° E, 0–20° N), **h** Southern Africa (12.5–40° E, 5S–35° S), (i) Central Eurasia (30–97.5° E, 42.5–72.5°N), **j** the Middle East (30–65° E, 23–40° N), **k** Northern India (75–87.5° E, 22.5–32.5° N), **l** Northeast China (110–127.5° E, 35–47.5° N), **m** Japan(122.5–127.5° E, 22.5–27.5° N; 127.5–132.5° E, 25–32.5° N; 132.5–140° E, 30–40° N; and 140–145° E, 40–45° N), **n** Siberia (100–170° E, 55–72.5° N), **o** Northwest Australia (115–137.5° E, 30–10° S), and **p** Eastern Australia (140–155° E, 17.5–40° S)

1966 and 1973–1976) (Fig. 4c), while an increasing trend from 1954 to 1993 is evident in the streamflow (and precipitation) for the Mississippi river (Fig. 4f). In general, large year-to-year fluctuations overshadow any long-term changes in the streamflow records, although some multi-decadal and long-term trends are evident in some of the time series (e.g., for Congo, Orinoco, and Mississippi).

Continental freshwater discharge into the oceans represents a major water flux of the global water cycle that returns the water vapor flux transported from the oceans to land by winds back to the oceans (Trenberth et al. 2007).
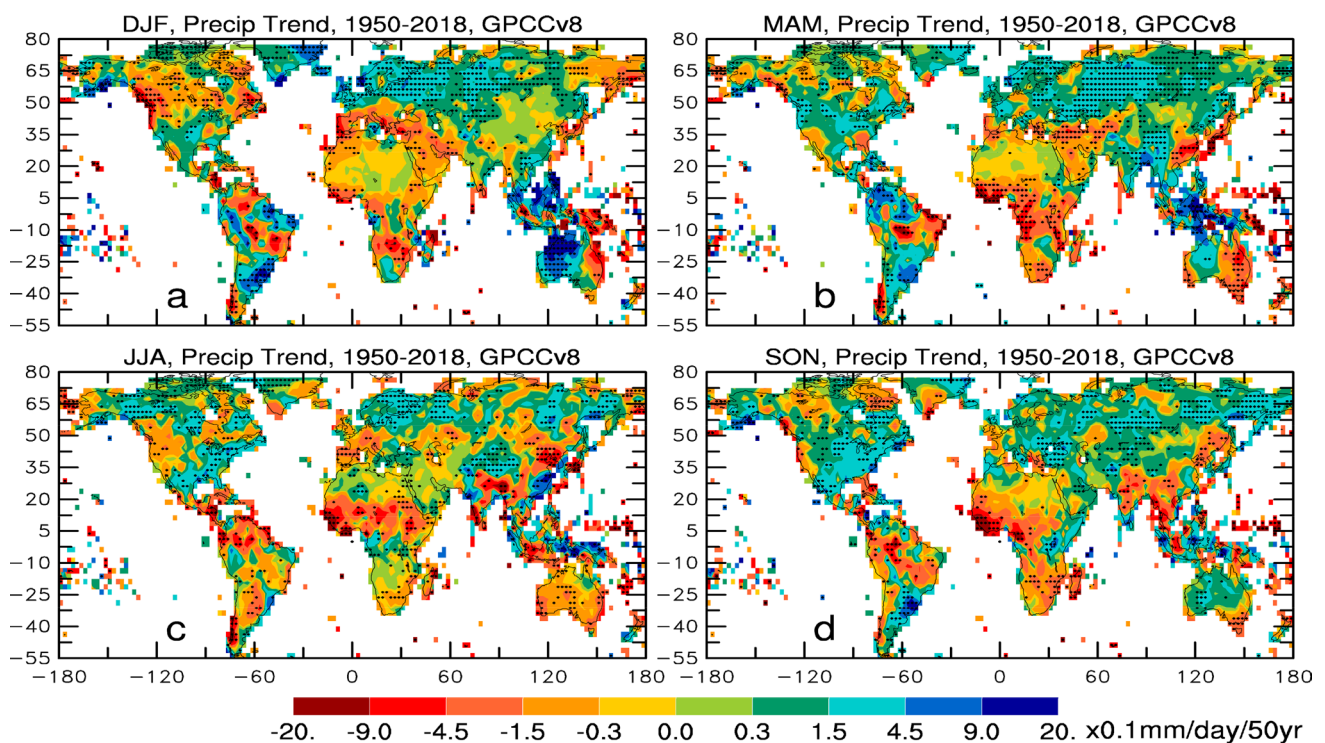
Fig. 2 Same as Fig. 1a but for seasonal precipitation trends based on the GPCP v8 dataset (data for 2017–2018 were based on GPCP v2.3)
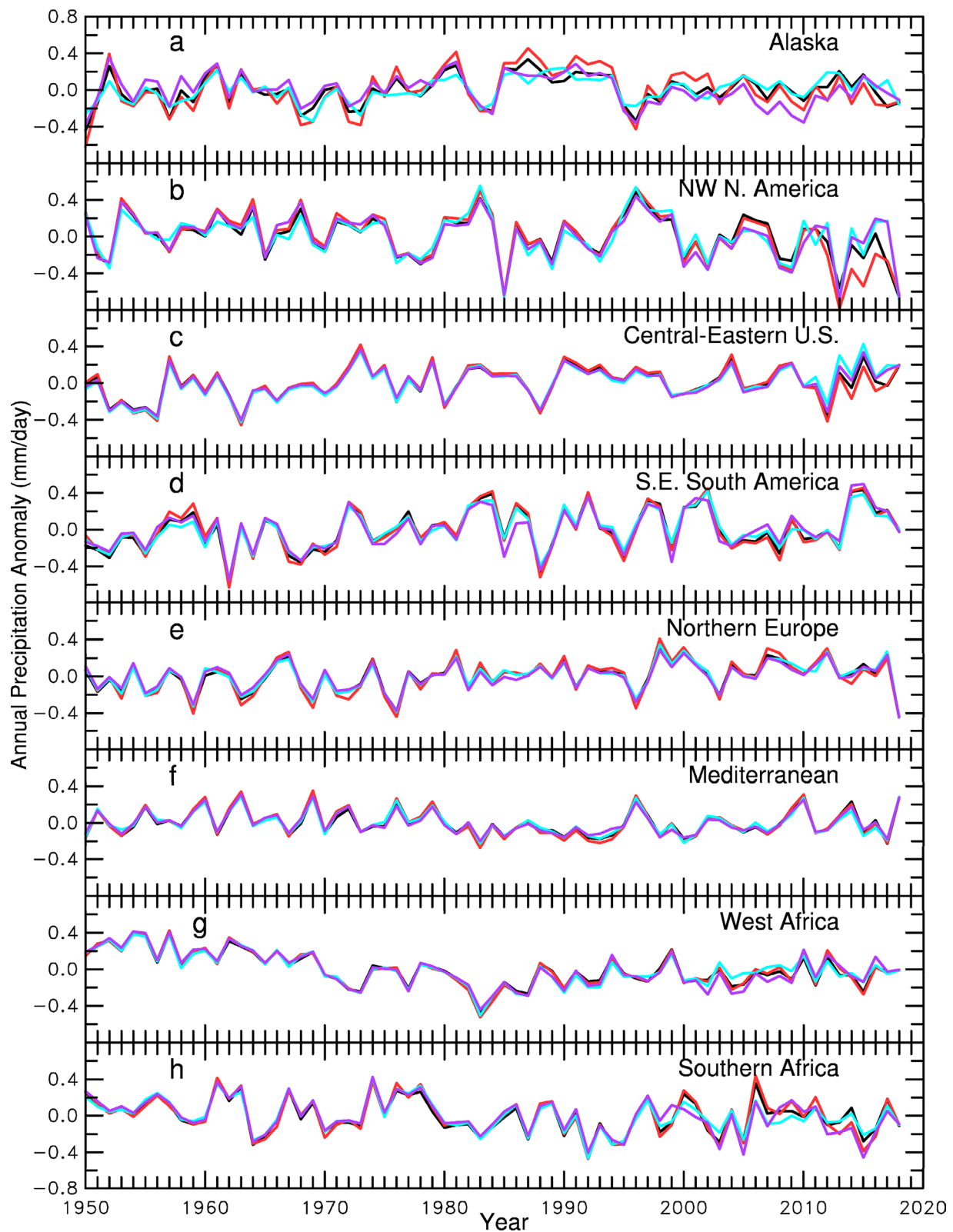
It also represents the renewal freshwater resource available to all inhabitants on land (Dai et al. 2009). Thus, variations and long-term changes in continental discharge have major implications to the global water cycle (e.g., the accumulation of water on land or in the oceans), sea-level rise and human society. Figure 5 updates the estimate of
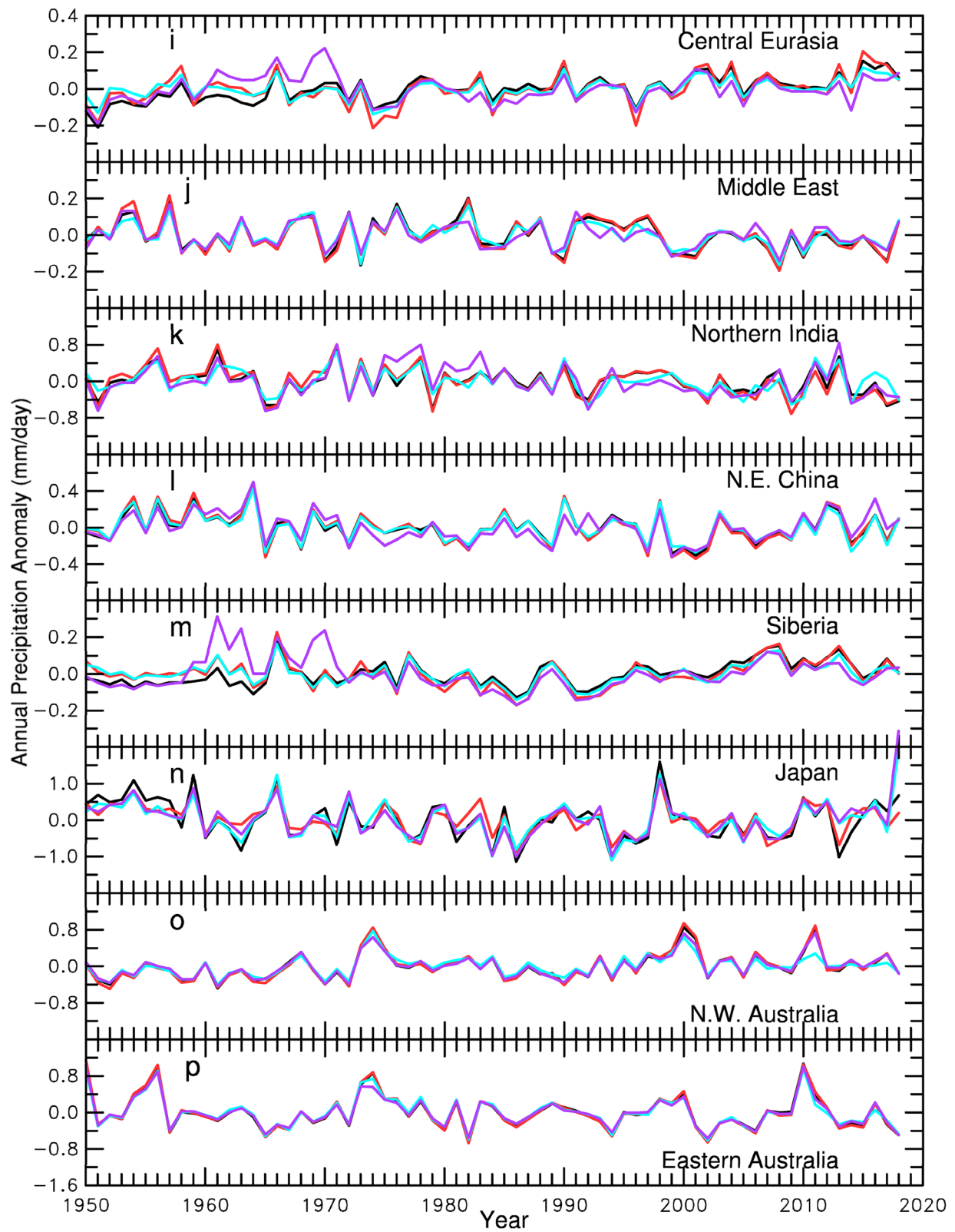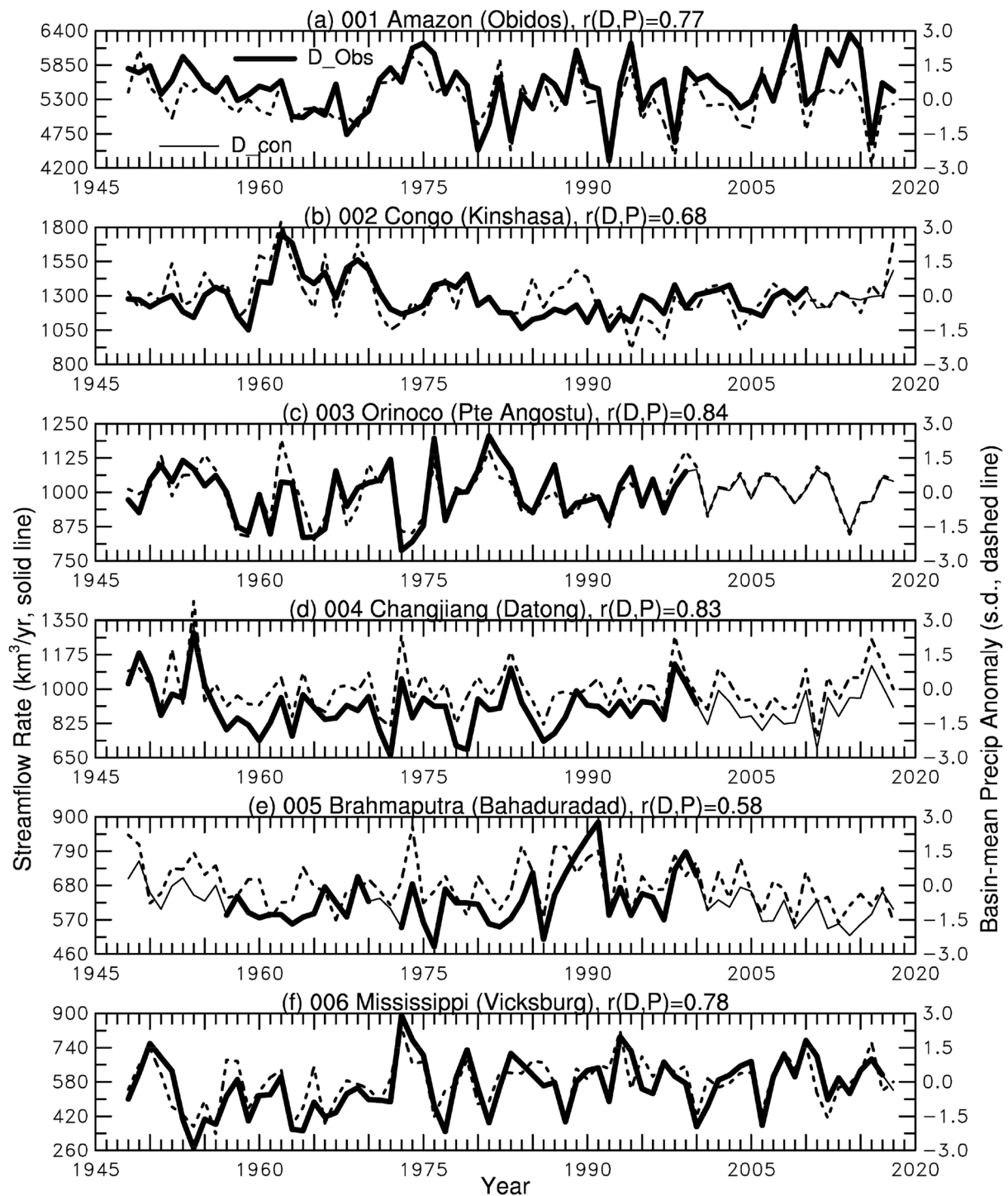
Fig. 3 (continued)

Fig. 4 Time series from 1948–2018 of yearly (October of the previous year–September of the plotted year) mean streamflow rate (in km^3 year^{-1}) from observations (thick solid line) and estimated using basin-mean PDSI or precipitation (thin solid line) at the farthest downstream station for world's six largest rivers, with the river name (station name) shown on top of each panel. Also shown (dashed line) is the basin-averaged precipitation anomaly (right ordinate, normalized by its standard deviation) from GPCC v8. The correlation r (D, P) between the thick solid and dashed lines is also shown

the global continental freshwater discharge of Dai et al. (2009) and Dai (2016) using the updated streamflow data (for 261 largest rivers) and the updated precipitation or scPDSIpm data (for other 146 rivers) that is correlated with streamflow and thus is used to extend or infill the gaps in the streamflow gauge records (cf. Fig. 4). As noticed
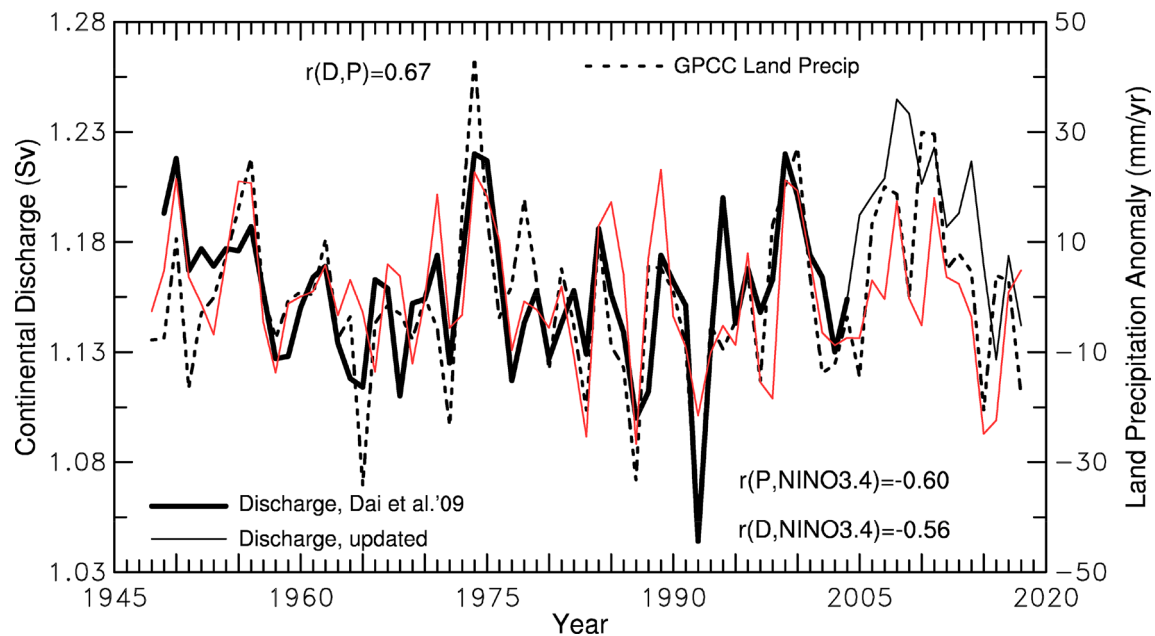
Fig. 5 Yearly time series of October–September mean total continental discharge (in Sv or 1×10^6 m³ s⁻¹, excluding that from Greenland and Antarctica) from 1949–2004 (thick solid line) estimated based on streamflow observations from 925 world's largest rivers (from Dai et al. 2009), and for 2005–2018 (thin solid line) estimated based on updated streamflow data for 407 of world's largest rivers and a linear regression with the think solid line. The dashed line is the Octo-ber–September mean precipitation averaged over global (60° S–75° N) land areas. The red line is the Nino3.4 (170° W–120° W, 5° S–5° N) SST index (positive downward, range from −3.0 to +3.0). Also shown are the correlation coefficients between the discharge (D), precipitation (P) and Nino3.4 index. The x axis indicates the year of the September (e.g., 1948 refers to the average for 10/1947-9/1948)

previously (e.g., Dai et al. 2009), continental discharge is highly correlated with land precipitation (r = 0.67) during 1948–2018, and they both correlate negatively with the Niño3.4 sea surface temperatures (SSTs) (r ≈ − 0.60) (Fig. 5). That is, land precipitation and continental discharge tend to be below (above) normal during warm El Niños (cold La Niñas), as these events affect precipitation over many land areas (Dai and Wigley 2000). In particular, since 2011 the Niño3.4 SSTs have increased, leading to below normal land precipitation and discharge for the recent several years. While large multi-year variations dominate the Niño3.4 index and the land precipitation and discharge time series, decadal to multi-decadal variations (referred to as the Interdecadal Pacific Oscillation or IPO, Dong and Dai 2015) are evident in Fig. 5, with below-normal (above-normal) land precipitation and discharge during the IPO warm phrase from 1977 to 1998 (cold phases from 1948 to 1976 and from about 1999–2014). Thus, the IPO's influences on regional precipitation over the U.S. (Dai 2013b) and other regions (Dong and Dai 2015) lead to decadal-multidecadal variations in global land precipitation and continental discharge with below-normal (above-normal) values during IPO's warm (cold) phases. The return to cold SST anomalies after the strong 2015/2016 El Niño suggests that the IPO's current cold phase, which started around 1999, may not be over yet,

as the previous cold phase lasted for about 31 years from 1946 to 1976 with reduced SST negative anomalies from the late 1950s to middle 1960s (Dai 2013).

3.2 Historical drying trends in scPDSIpm

To understand the long-term changes in scPDSIpm, in Fig. 6 we plotted the global land-averaged meteorological variables whose gridded values were used to calculate the local scPDSIpm. For surface air temperature (Tas), the variations and changes are very similar among three datasets, and thus we only used the CRUTEM4 (with its gaps infilled with data from CRU TS4.02) Tas data in the calculation. For precipitation, four datasets were used to create different versions of the scPDSIpm with the other forcing data being the same. The other forcing data include surface net radiation, which requires estimates of the surface longwave and shortwave radiation, with the latter being estimated based on cloud cover data (Fig. 6d) from CRU TS4.02 (see Dai and Zhao 2017 for details). Besides precipitation, the other important driver of the scPDSIpm is the surface vapor pressure deficit (VPD, Fig. 6e), which was derived based on the CRU TS4.02 vapor pressure and Tas data. Figure 6f also shows the PET calculated using these forcing data (plus surface wind speed data from the 20th century reanalysis, see Dai and Zhao 2017) and the
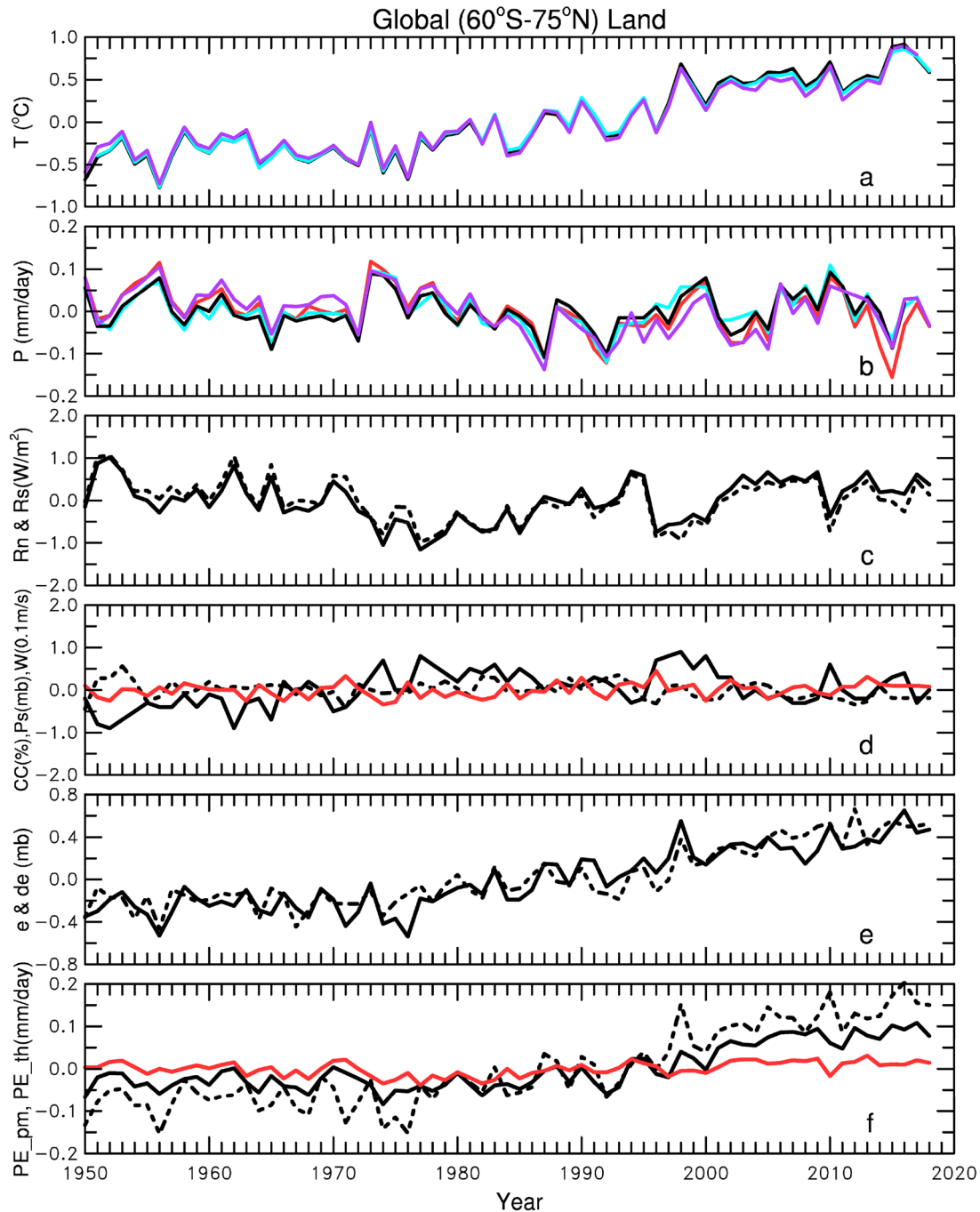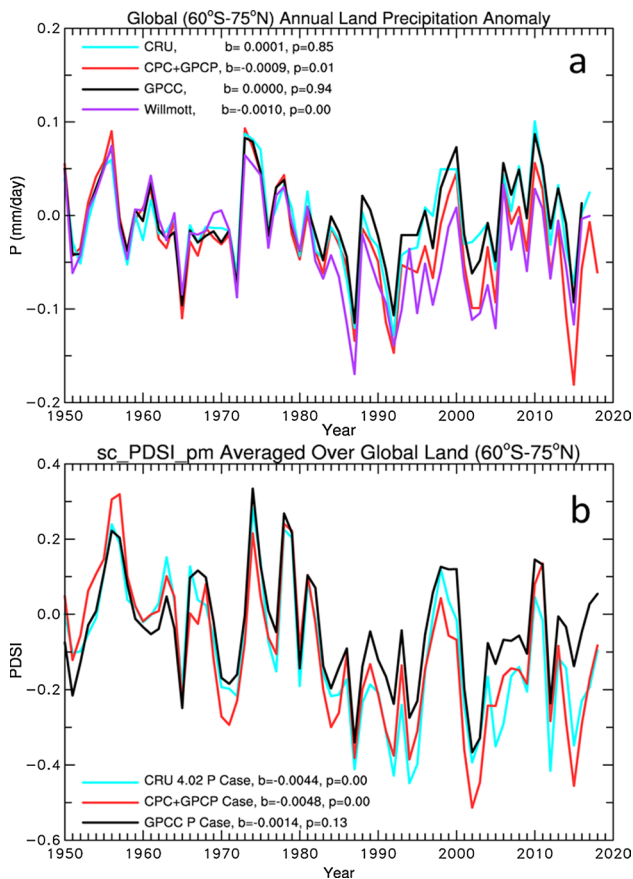
Fig. 6 Globally (60° S–75° N)-averaged annual anomaly (relative to 1950–2018 mean) time series of the meteorological forcing data over land used in this study: **a** surface air temperature [three lines overlap each other: black = CRUTEM4 (Osborn and Jones 2014), blue = CRU TS4.02 (Harris et al. 2014), magenta = Univ. of Delaware or UDel T), **b** precipitation (black = GPCC v8, blue = CRU TS4.02, red = DaiP, magenta = UDel), **c** surface net radiation (solid) and surface net solar radiation (dashed), both positive downward, **d** cloud cover (black solid), surface air pressure (black dashed) and wind speed (red), **e** surface air vapor pressure (solid) and vapor pressure deficit (dashed), and **f** calculated PET_pm (black solid), PET_th (black dashed, i.e., PET from the Thornthwaite Eq. see Dai 2011b), and the PET_pm with constant T and vapor pressure (red)

Penman-Monteith equation (PET_pm) or the Thornthwaite equation (PET_th) (see Dai 2011b for details), as the PET is a critical factor in the Palmer model (Palmer 1965) used to calculate the PDSI.

Figure 6 shows that while surface radiation exhibits some decadal and multi-year variations (e.g., low values from 1972 to 1985 and 1996–2000) associated with cloudiness changes, significant long-term trends exist mainly in

Fig. 7 **a** Globally (60° S–75° N)-averaged annual land precipitation anomaly (relative to 1950–1979 mean) from 1950 to 2018 calculated using the CRU TS4.02 (blue), CPC (for 1950–1978) plus GPCP v3 (for 1979–2018) (red), GPCC v8 (black), and Willmott or UDel (magenta) dataset. The slope (b, mm/day per year) and its p-value are also shown for each line. **b** Globally (60° S–75° N)-averaged annual scPDSIpm time series from 1950 to 2018 calculated using the same meteorological forcing data (from CRU TS4.02) except for precipitation, which was from CRU TS4.02 (blue), GPCC v8 (black), and CPC + GPCP (red). The slope (**b**, change per year) and its p value are also shown for each line. The UDelP case has a slope of − 0.008 (p = 0.00) with much larger decreases for scPDSIpm and is not shown in **b**

the VPD associated with rising Tas coupled with small changes in surface relative humidity (Dai 2006; Willett et al. 2019). The rising Tas and VPD lead to large increases in PET, especially in PET_th, which tends to overestimate the impact of surface warming on PET and thus on PDSI (Burke and Brown 2008; Dai 2011b; van der Shrier 2011). Thus, any long-term drying trends in the calculated scPDSIpm is likely caused by surface warming and the associated increase in PET, although below-normal precipitation in the 1980s and 1990s, early 2000s, and around 2015 (due to the strong 2015/2016 El Niño, Fig. 5) also contributes to the dry conditions in these years (Fig. 7). As shown in Fig. 1, significant drying trends occurred over Africa, East Asia,

southern Europe, eastern Australia and other regions, but they are partially offset by the wetting trends over central and northern Eurasia, the central US, Northwest Australia and other areas. As a result, the global-mean scPDSIpm (Fig. 7b) shows only a small decreasing (i.e., drying) trend from 1950 to 2018 (mainly from the early 1970s to middle 1990s). The global-mean scPDSIpm shows large interannual variations that are caused primarily by land precipitation variations (Fig. 7) associated with El Niño-Southern Oscillation (ENSO) events (Fig. 5). Substantial differences exist among the four land precipitation products since the middle 1990s (Fig. 7a) due to the large decline in the number of rain-gauges with data (Sheffield et al. 2012; Trenberth et al. 2014), with the GPCP v2.3 (used by DaiP) and UDelP being drier than the GPCCv8 and CRU TS4.02. These P differences contribute to the scPDSIpm differences for the recent 20–30 years, with the GPCCv8 case being wetter relative to the CRU and DaiP cases (Fig. 7b). Nevertheless, the drying trend from the early 1970s to middle 1990s is evident in all the precipitation cases, although the global-mean aridity conditions may differ substantially for the recent years when different precipitation products are used. This suggests that improvements to global land precipitation products are needed for the period since the middle 1990s.

Besides the declining precipitation over Africa and many other regions (Fig. 1a), rising Tas over land, especially over central and northern Eurasia, Alaska and northern Canada (Fig. 8c) is also driving up the PET (Fig. 6f), which in turn causes scPDSIpm to decrease (Fig. 8a, b). The surface warming is most pronounced since the late 1970s (Fig. 6a), when the drying effect of the warming becomes evident (Fig. 8a). Thus, the scPDSIpm trends shown in Fig. 1c, including the drying trends over East Asia, southern Europe, and parts of North America, result partly from the drying trend caused by the recent surface warming, although precipitation changes still dominate the scPDSIpm trends over central and northern Eurasia, Africa, South America, and Australia.

On decadal and longer time scales, the scPDSIpm from 1920 to 2018 shows a long-term trend (drying over most of Africa, South and East Asia, southern Europe and wetting over most of the northern mid-high latitudes and Northwest Australia) that is associated with global warming (thus it is largely forced by GHG increases), together with a multi-decadal mode (i.e., MCA2) that is associated with the multi-decadal variability in Pacific and North Atlantic sea surface temperatures (Fig. 9). The spatial patterns of the second mode (Fig. 9c) resemble those of the IPO in the Pacific (Dai 2013b; Dong and Dai 2015) and the Atlantic Multidecadal Variability (AMV) in the Atlantic (Enfield et al. 2001), and its temporal evolution (Fig. 9b) is correlated with the IPO (r = 0.79) and AMV (r = 0.58) during 1920–2014. Together, the IPO and AMV explain 90 % of the temporal variations

Fig. 8 **a** Globally (60° S–75° N)-averaged annual scPDSIpm time series from 1950 to 2018 calculated using the same CPC + GPCP precipitation data and the same meteorological forcing data from CRU TS4.02 except for surface air temperature (T) and vapor pressure (e) changes: the red line is with the T and e changes while the black line is without these changes, i.e., climatological values were used for T and e for the black line. **b** Distributions of the 1950–2018 trend difference between the scPDSIpm with and without the T and e changes. **c** The T 1950–2018 trend map based on the CRU TS4.02 dataset
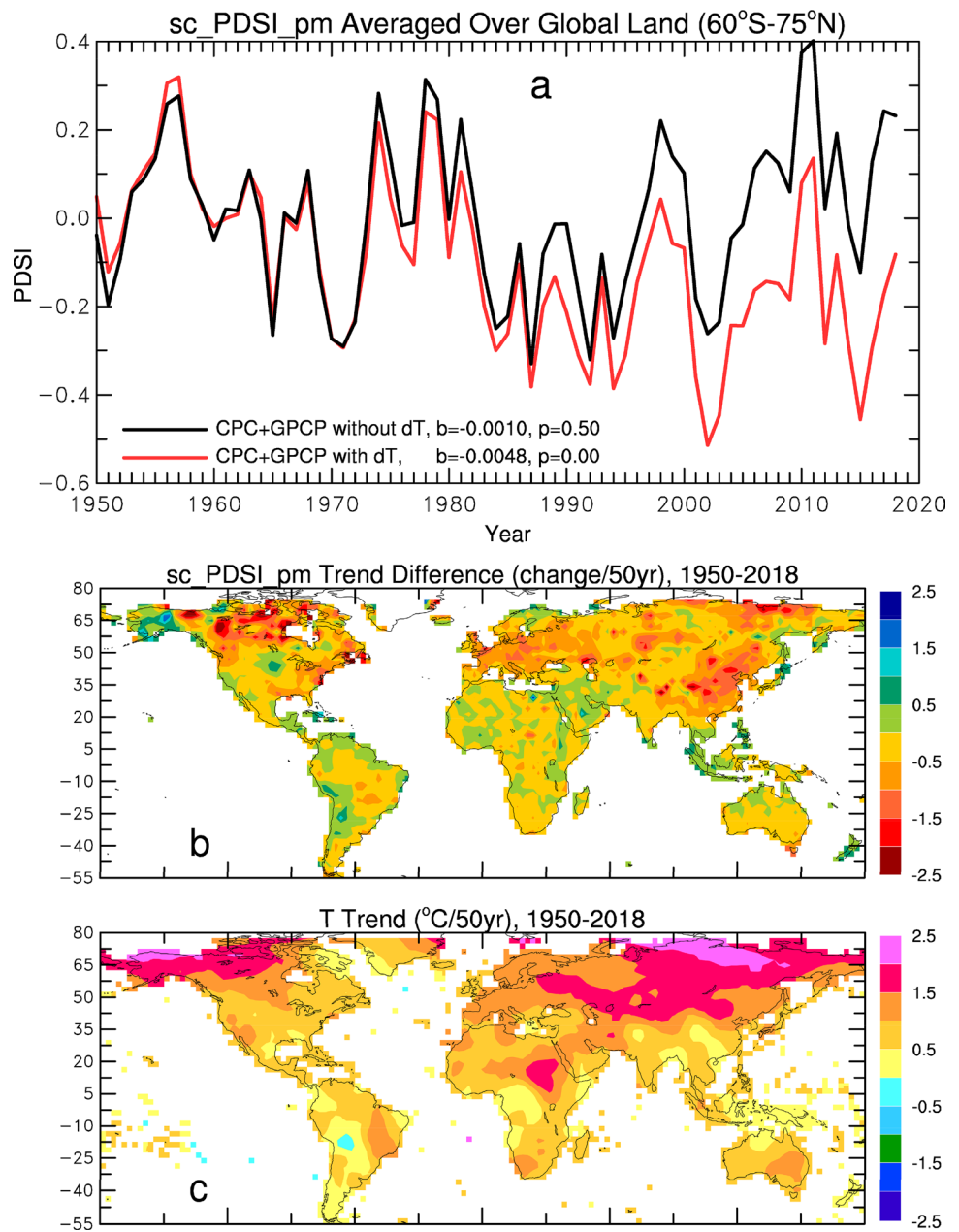
of the second mode (Fig. 9b). Thus, this multidecadal mode is associated with the IPO and AMV, which are thought to originate from oceanic processes and air-sea interactions (Liu 2012). Therefore, we may consider the associated scP-DSIpm mode (Fig. 9b,f) as being caused by the IPO and AMV. This mode shows that, on top of the long-term trend represented by the first mode (Fig. 9a,d), the period from about 1975–1998 was relatively dry (wet) over the Sahel, northeastern Asia, Alaska and northern Canada (southwestern North America, most of South America, the Middle East, and most of Europe and Australia); whereas it is the opposite for the periods from about 1945–1974 and since about 1999 (Fig. 9b,f). While the IPO since 1920 resulted primarily

from internal variability (Hua et al. 2018), the recent AMV may have partly resulted from decadal variations in volcanic and anthropogenic aerosols (Qin et al. 2020b). Thus, the multi-decadal mode (i.e., MCA2) shown in Fig. 9 may have partly resulted from aerosol forcing, besides the contribution from the internal SST variability in the Pacific (i.e., IPO) and Atlantic (i.e., the internal component of the AMV, Qin et al. 2020b).

On interannual to multi-year time scales, the scPDSIpm is dominated by ENSO (Fig. 10a,c,d)., which causes wet conditions over southwestern North America, southern South America, southwestern Asia but dry conditions over Australia, the maritime continent, South Asia, northern South America,
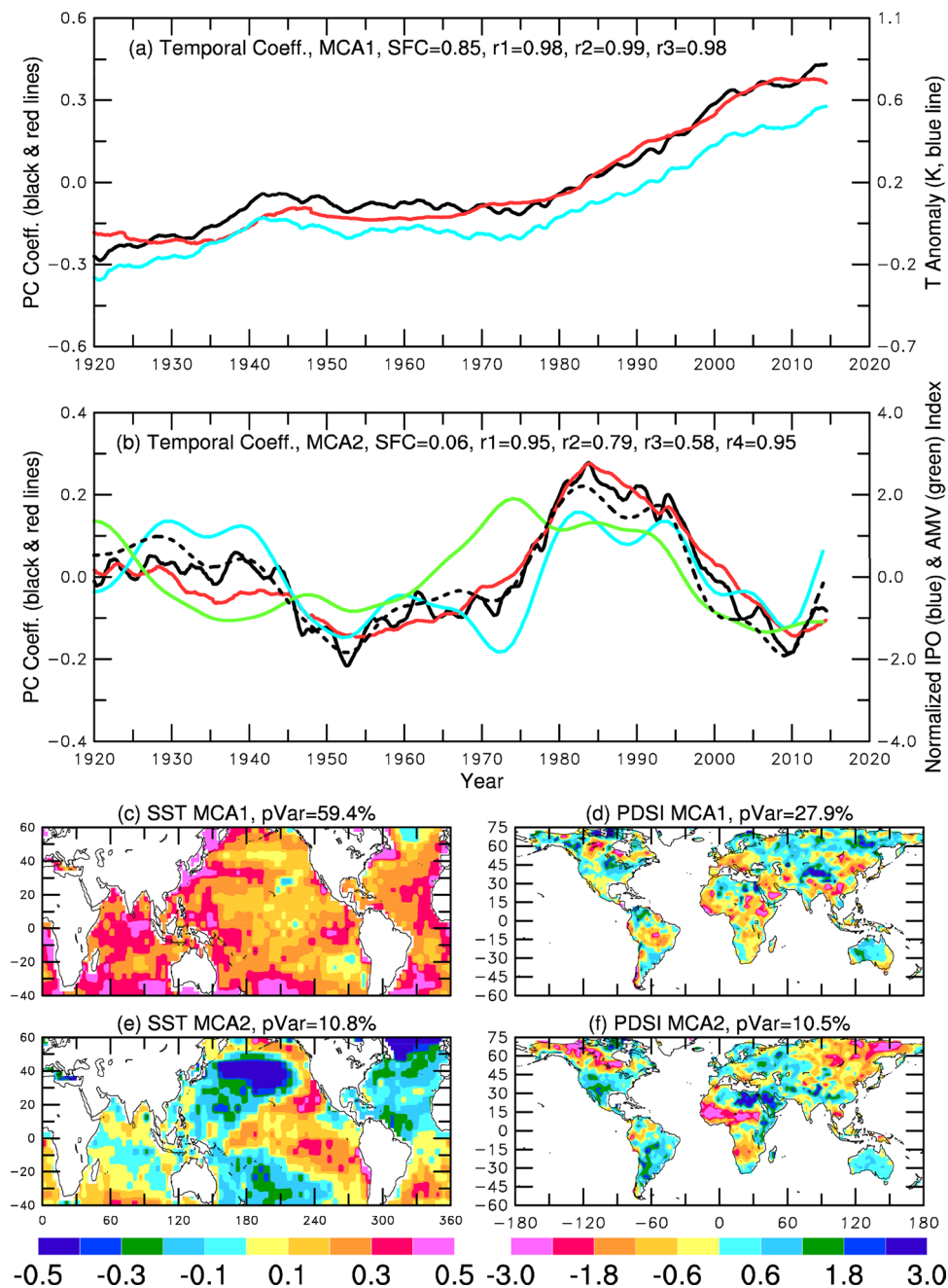
Fig. 9 Temporal (**a**, **b**, black for SST, red for scPDSIpm) and spatial (**c–f**) patterns of the two leading modes from a maximum covariance analysis (MCA, Bretherton et al. 1992) of the observed SST (from HadSST3, Kennedy et al. 2011) and the DaiP-based scPDSIpm from 1920–2018. Panels **a**, **c** and **d** are for the first MCA mode (MCA1) and **b**, **e** and **f** are for the second MCA mode (MCA2). Nine-year moving-averaged data were used in the analysis. The blue line in **a** is the similarly smoothed global-mean surface temperature anomaly (on the right y-axis) obtained from the Climate Research Unit (CRU, http://www.cru.uea.ac.uk/cru/data/temperature/HadCR UT4-gl.dat, Osborn and Jones 2014). The dashed black line in **b** is the estimated SST PC coefficient using a linear regression with the normalized IPO (blue, from Hua et al. 2018) and AMV (green, for a negative phase, from Qin et al. 2020b) indices: dashed black line = − 0.0006 + 0.0895*blue line + 0.0635*green line. In **a-b**, SFC is the squared fractional covariance explained by the MCA mode and the *r1* and *r2* are the correlation coefficients between, respectively, the black and red, and black and blue lines. *r3* is the correlation coefficient between the red and blue lines in **a** and the black and green lines in **b**. *r4* in **b** is the correlation coefficient between the solid and dashed black lines. *pVar* is the percentage variance explained by the MCA mode in **c–f**. The corresponding MCA modes depict the statistically associated temporal *and* spatial patterns in the SST and scPDSIpm fields. The product of the temporal and spatial coefficients at a given location is the SST or scPDSIpm anomaly represented by the MCA mode

Fig. 10 Same as Fig. 9 except for the two leading MCA modes of the high-pass filtered SST and scPDSIpm data; that is, the 109-month moving average was first removed from the monthly data and then the residuals were subjected to the MCA analysis. The r is the correlation coefficient between the black and red curves in **a, b**. The green curve in **a** is the similarly filtered Nino3.4 SST index. The blue curve in **a** is the black curve in **b** (i.e., the PC2 of SSTs) shifted backward by six months and smoothed using 7-month moving average. The r_1 (r_2) is the correlation coefficient between the black and green (blue) curves in **a**
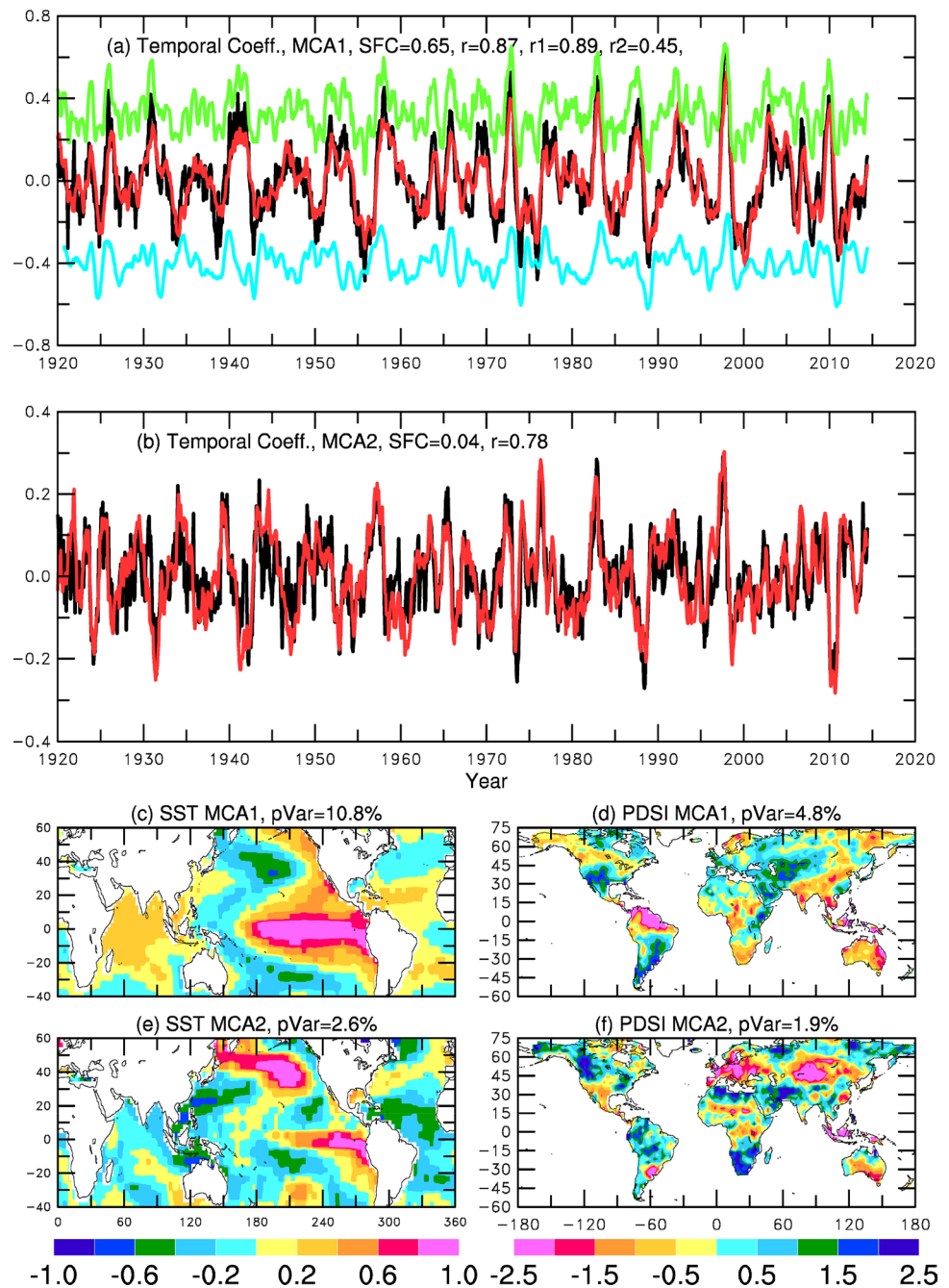
and southern Africa during El Niño, and the opposite during La Niña (Fig. 10d). Interestingly, there is another interannual mode (MCA2) with warm SST anomalies in both the equatorial eastern Pacific and northwestern Pacific and cold SST anomalies in the western Pacific and tropical Atlantic that lag the ENSO mode by about six months (Fig. 10b,e). Thus, the SST anomalies of this mode peak around May-June following the December-January peak of the ENSO event (Fig. 10a). This suggests that this mode is also likely related to ENSO,

despite its non-conventional ENSO-like SST patterns and the delayed temporal evolution. Associated with this SST mode, the scPDSIpm anomalies show quite different patterns compared with those associated with typical ENSO, with dry conditions over central Asia, most Europe, and southeastern Australia but wet conditions over Alaska and western Canada, most of South America, southern Africa, the Middle East and northeastern Asia (Fig. 10f).
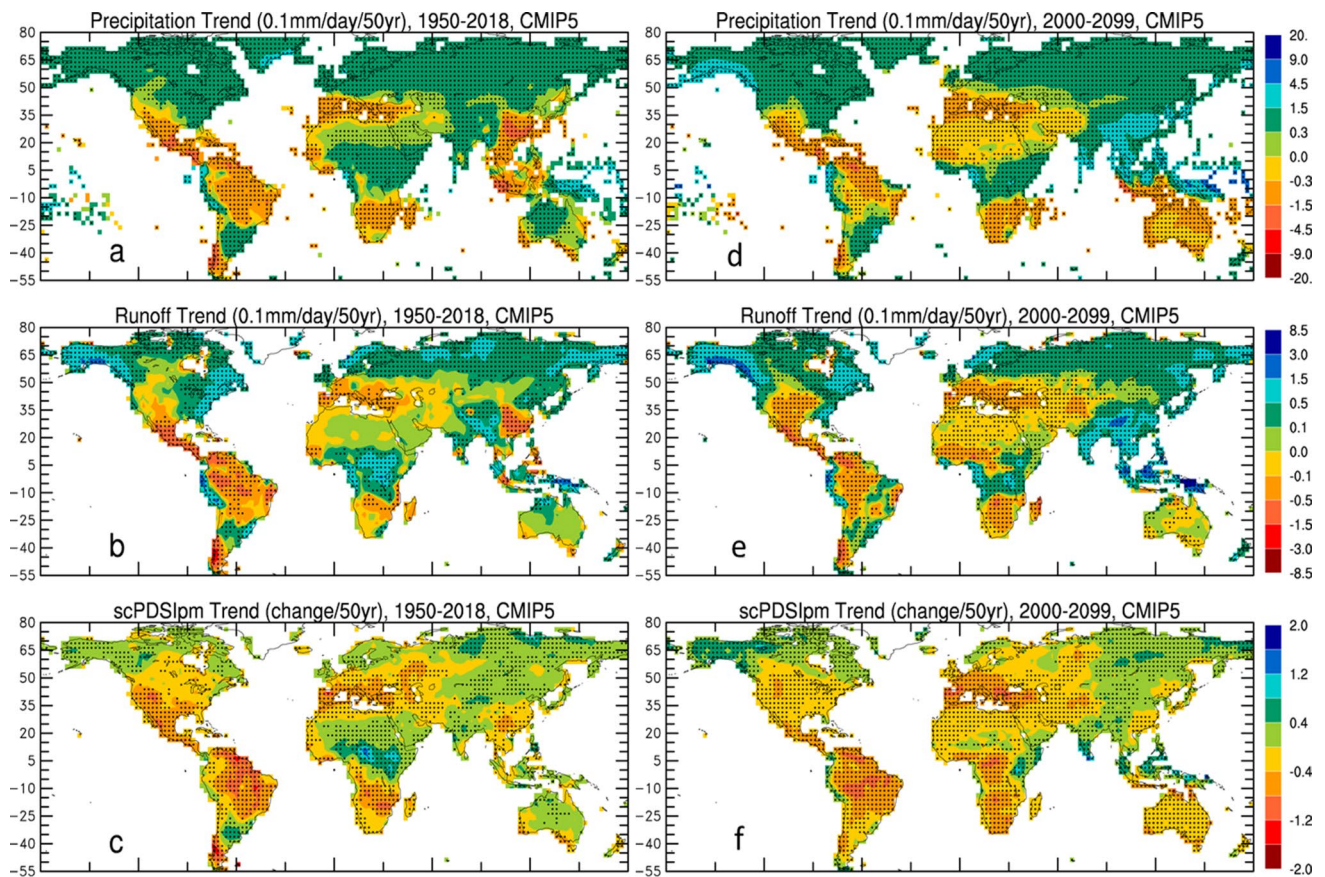
Fig. 11 a–c Same as Fig. 1 except for the trends in the ensemble mean of **a** annual precipitation from 81 runs from 40 CMIP5 models, **b** total runoff from 66 runs from 33 CMIP5 models, and **c** scPDSIpm calculated using data from 14 runs from 14 CMIP5 models. The historical all-forcing (for 1950–2005) and the RCP4.5 scenario (for 2006–2018) are used for the model simulations. The data are masked to have similar spatial coverage as in Fig. 1. **d–f** Same as **a–c** except for trends during 2000–2099 under the RCP4.5 scenario. Each row shares the color bar on the right side, with the units shown on top of the panels

## 4 Comparison with CMIP5 model-simulated trends

4.1 Differences in model-simulated historical and future trends

Before comparing with the trends estimated from observational data, we first examine the model-simulated ensemble-mean trends from 1950 to 2018 and from 2000 to 2099 for annual precipitation, runoff, and scPDSIpm in Fig. 11. The ensemble averaging over multi-model simulations smooths out most of the regional variations caused by internal variability, making Fig. 11 much smoother spatially than Fig. 1. The drying reflected by the scPDSIpm trend (Fig. 11c) is more widespread than that seen in precipitation or runoff trend (Fig. 11a, b), mainly due to the additional drying caused by increased PET under rising air temperatures (Zhao and Dai 2015). Many of these historical trend patterns are consistent with those expected to occur in the 21st century under increasing GHGs (Fig. 11d, f; Collins et al.

2013; Zhao and Dai 2015, 2017; Dai et al. 2018), such as the increased (decreased) precipitation, runoff and scPD-SIpm over most of North America and Eurasia (Southwest North America, northern and central South America, the Mediterranean region, and southern Europe). However, the large precipitation and runoff decreases over Southeast Asia during 1950–2018 are absent in the projected future changes (Fig. 11). Furthermore, compared with the changes in the 21st century from the same model runs (Fig. 11d, f) and other CMIP5 models (Collins et al. 2013; Dai et al. 2018), over Northwest Australia precipitation and runoff increase during 1950–2018 whereas precipitation decreases and runoff changes little there in the 21st century, and the drying over southern Brazil during 1950–2018 is more intense and widespread than in the 21st century while it is the opposite for northern Africa (Fig. 11).

Seasonal precipitation trend maps for 1950–2018 from the CMIP5 MMM (Fig. 12a–d) show patterns similar to those for annual precipitation (Fig. 11a), except that the wetting trend over Northwest Australia is most pronounced in
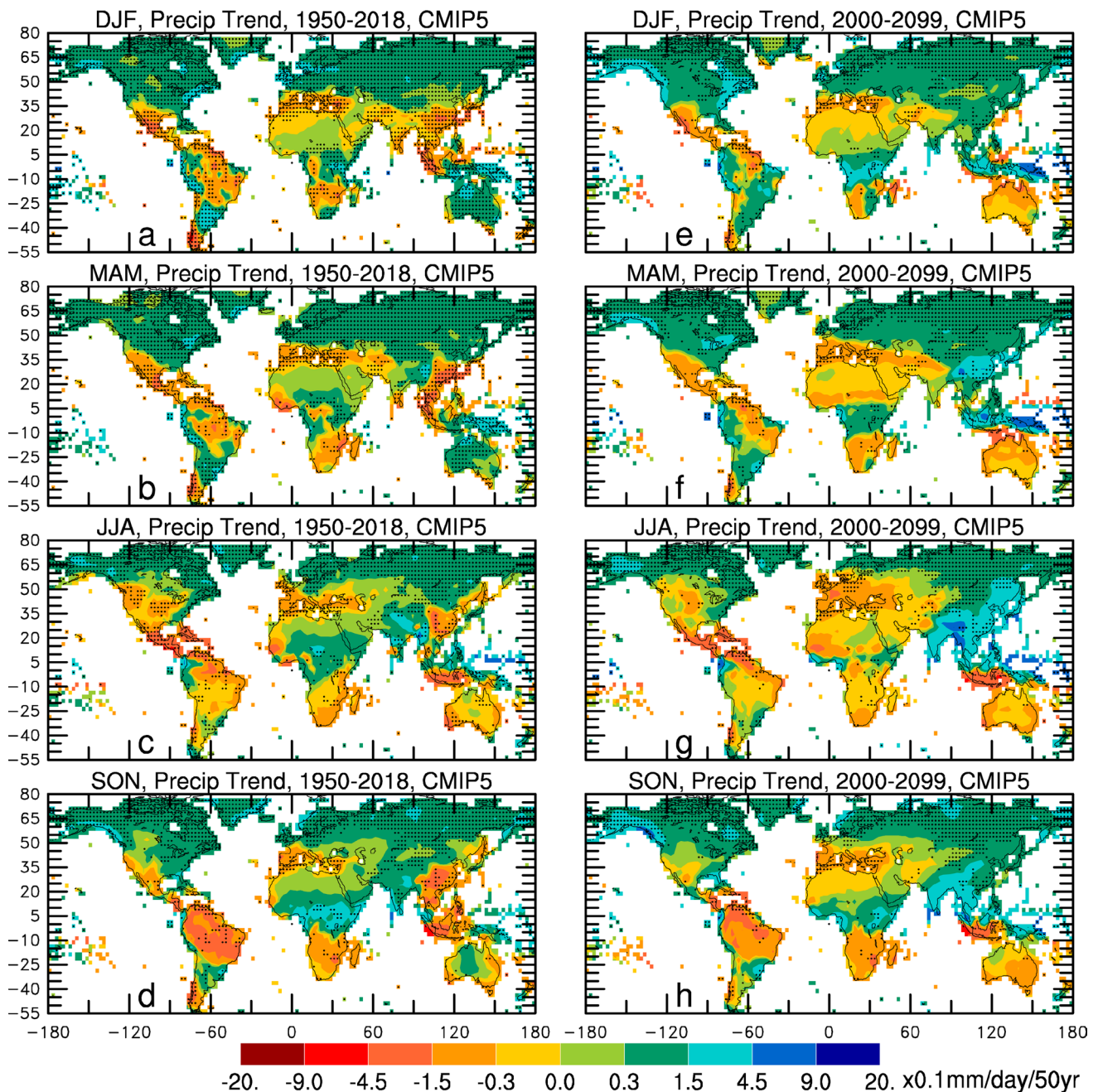
Fig. 12 Linear trend maps in seasonal precipitation from the ensemble mean of 81 runs from 40 CMIP5 models during 1950–2018 (left column) and 2000–2099 (right column, RCP4.5 scenario)

DJF and MAM but absent in JJA. The drying over Southeast Asia and northern-central South America is seen over all seasons, especially in SON for the South American drying (Fig. 12d). The drying over Central America is largest in JJA but lest in SON (Fig. 12c–d). In contrast, during the 21st century (Fig. 12e–h) precipitation decreases over Australia and increases in Southeast Asia in all seasons, while precipitation over southern Brazil increases in DJF. Furthermore, the drying over Europe, the Middle East and northern Africa

in JJA and MAM is more widespread in the 21st century than during 1950–2018 (Fig. 12). Thus, large differences in the model-simulated precipitation response to external forcing between 1950–2018 and 2000–2099 exist over Australia (mainly in DJF and MAM), Southeast Asia (in all seasons), and a few other places.

The above regional differences in the model-simulated responses to external forcing between 1950–2018 and the 21st century may partly result from the different aerosol

forcing during the two periods, since historical anthropogenic and volcanic aerosols, which differ in the RCP4.5 scenario for the 21st century, may have played an important role in the recent surface warming in the North Atlantic (Booth et al. 2012; Murphy et al. 2017; Bellomo et al. 2018; Hua et al. 2019; Qin et al. 2020b) and other regions (Qin et al. 2020a), and that the aerosol forcing may have caused a drying trend since the 1970s over Southeast Amazon and a wetting trend over the Sahel in West Africa (Hua et al. 2019). The different precipitation responses over Southeast Asia and Northwest Australia between 1950–2018 and 2000–2099 may also be related to different aerosol forcing over East Asia. However, how the historical aerosol forcing has contributed to the drying over Southeast Asia and southern Brazil and the wetting over Northwest Australia requires further investigation.

### 4.2 Comparison between observed and model-simulated historical trends

Many of the observed trend patterns shown in Fig. 1 are qualitatively (and statistically) consistent with the model-simulated trends shown in Fig. 11a–c for the same period from 1950 to 2018. For example, increased precipitation and runoff and wetting trends of comparable magnitudes are seen in both observations and models over many northern mid-high latitudes, Northwest Australia, and southeastern South America; while decreased precipitation and runoff and drying trends are seen over southern Europe, southern Africa, and Southeast Asia. These consistent trend patterns suggest that GHG and other external forcing may have already caused detectable changes in these hydroclimatic fields during 1950–2018. On the other hand, some of the regional trends shown in Fig. 1 are likely caused by multi-decadal internal variations and thus are not directly comparable to the forced trends shown in Fig. 11a–c. A more precise assessment of the statistical consistency or inconsistency between the observed and model-simulated trends would require a comparison of the observed trends with the 5th -95th percentiles of the model-simulated trends at each grid point, as done in Knutson and Zeng (2018) for historical precipitation trends. Also, internal variability should have a larger impact on the seasonal trends shown in Fig. 2, making them less comparable with the forced trends shown in Fig. 12a–d.

To find out to what extent the trend patterns shown in Fig. 1 estimated from historical data, which include both externally-forced and internally-generated changes, are forced by external forcing, we used the SST field from the CMIP5 MMM as the forced response and performed an MCA analysis of the SST field together with the precipitation field from either CMIP5 MMM or observations. Figure 13 compares the leading MCA mode from these MCA analyses. Clearly, the MCA1 of the SST captures the global warming mode and it accounts for most (93.6%) of the smoothed SST's temporal-spatial variations during 1920–2018 (Fig. 13a–b). Associated with this warming mode, precipitation in the models shows a trend patten that resembles the linear trend pattern shown in Fig. 11a, with drying over some subtropical regions and Southeast Asia but wetting elsewhere (Fig. 13c). Associated with the warming mode, the MCA1 in observed precipitation from both the GPCC v8 and DaiP shows a similar long-term trend (Fig. 13a) with spatial patterns broadly consistent with the model-simulated precipitation response, with wetting over northern mid-high latitudes, Australia, and southeastern South America, but drying over parts of South Asia and Africa, and central South America (Fig. 13c–e). As the observed precipitation is from one single realization, it contains large unforced internal variations, leading to a much smaller fraction of the variance explained by this global warming mode than in the CMIP5 MMM (Fig. 13). Furthermore, the large internal variations make it difficult for the MCA technique to cleanly exact the forced precipitation component from other changes at many locations (such as West Africa and East Asia) where precipitation's internal variability is large. This is particularly true for the weaker forced signal represented by the second and third MCA modes of precipitation (figure not shown), which show consistent temporal coefficients but with different regional patterns between the CMIP5 MMM and observations.

For 9-year smoothed scPDSIpm, the first MCA mode is associated with the global warming (Fig. 14a), whose spatial patterns (Fig. 14d) resemble the trend map shown in Fig. 11c. This long-term trend mode is seen in historical scPDSIpm calculated based on either GPCC v8 P or DaiP, except over southwestern North America and northern Africa (Fig. 14a,d,g). The second and third MCA modes show multi-decadal changes over Africa, East Asia, and North America and other regions (Fig. 14b,c,e,f), which are likely forced by decadal variations in external forcing, such as anthropogenic and volcanic aerosols (Qin et al. 2020a, b). Many of these multi-decadal variations are evident in the historical scPDSIpm data (Fig. 14b,c,h,i), although noticeable differences exist (e.g., over South Asia for MCA2, and over Africa for MCA3), again likely due to sampling errors (i.e., impact of internal variability) in the estimated MCAs for the historical scPDSIpm data.

In summary, the linear trend patterns (Figs. 1 and 11a–c) and the MCA patterns (Fig. 13) suggest that the recent wetting (drying) trends over northern mid-high latitudes, Northwest Australia, and southeastern South America (southern Europe, Southeast Asia, and West and southern Africa) seen in historical data may be partly forced by external forcing; while the wetting trends over Southwest North America and
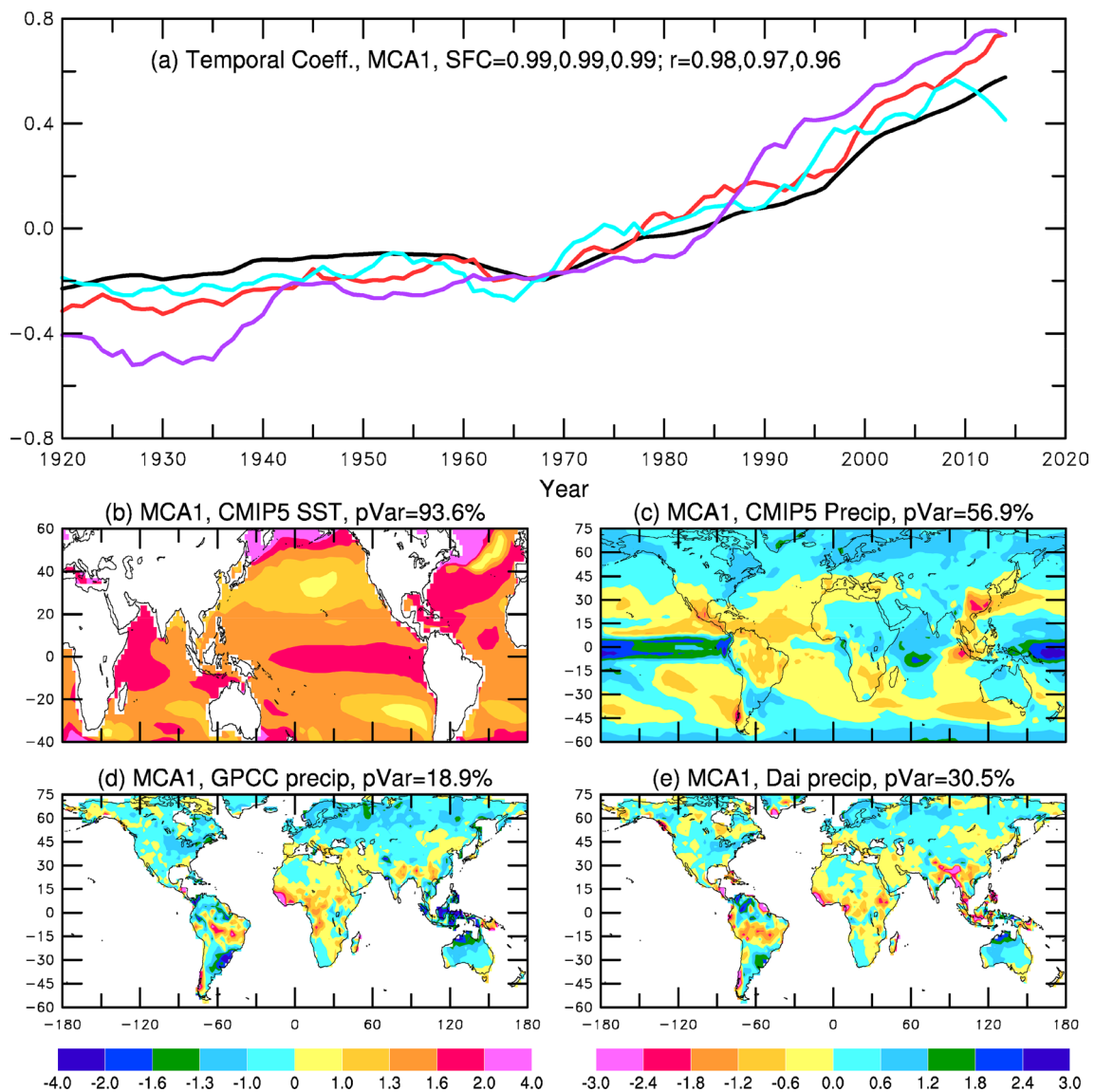
Fig. 13 Same as Fig. 9 except for the leading MCA mode of the 9-year smoothed annual SST (black line in **a**) from the multi-model ensemble mean (MMM) of the 68 all-forcing runs by 34 CMIP5 models and precipitation (red line in **a**) from the MMM of the 81 all-forcing runs from 40 CMIP5 models. The CMIP5 all-forcing historical runs were extended to 2018 using the corresponding RCP4.5 runs. The leading MCA mode of the same CMIP5 SST and 9-year smoothed precipitation from GPCC v8 (blue line in **a**, and **d**) or DaiP (magenta line in **a**, and **e**) is also shown, with its temporal and spatial patterns for SST are similar to those shown in **a** and **b**. The *r* in **a** is the correlation coefficient between the black line and red, blue, or magenta line, respectively. Panel **b** uses the left color bar while panels **c–e** use the right color bar

drying trend over eastern Australia may be mainly related to IPO and other internal variability.

5 Summary and discussion

In this study, I have updated our streamflow and scPDSIpm datasets to December 2018 and used the updated data to present a synthesized picture of the changes from 1950 to 2018 in land precipitation, streamflow, and scPDSIpm, an improved form of the PDSI that measures surface dryness or aridity relative to local mean conditions. A comparison with the CMIP5 model-simulated response to historical forcing is also made to assess how much of the historical changes may be forced by historical external forcing. In general, the rain-gauge and streamflow records from independent measurements show consistent change patterns, thus increasing our confidence in these historical data. Together, the raingauge and streamflow data suggest increased precipitation and runoff from 1950 to 2018 over mid-high latitude Eurasia,

Fig. 14 Same as Fig. 9 except for the three leading MCA modes of the 9-year smoothed annual scPDSIpm based on the GPCC v8 precipitation (red in **a–c**, and **g–i)** or DaiP (blue line in **a–c**) and from the multi-model ensemble mean (MMM) (black line in **a–c**, and **d–f**) of the scPDSIpm from 14 CMIP5 models. The CMIP5 all-forcing historical runs were extended to 2018 using the corresponding RCP4.5 runs. The SFC, *r* and pVar from the model versus DaiP case are shown in the parentheses
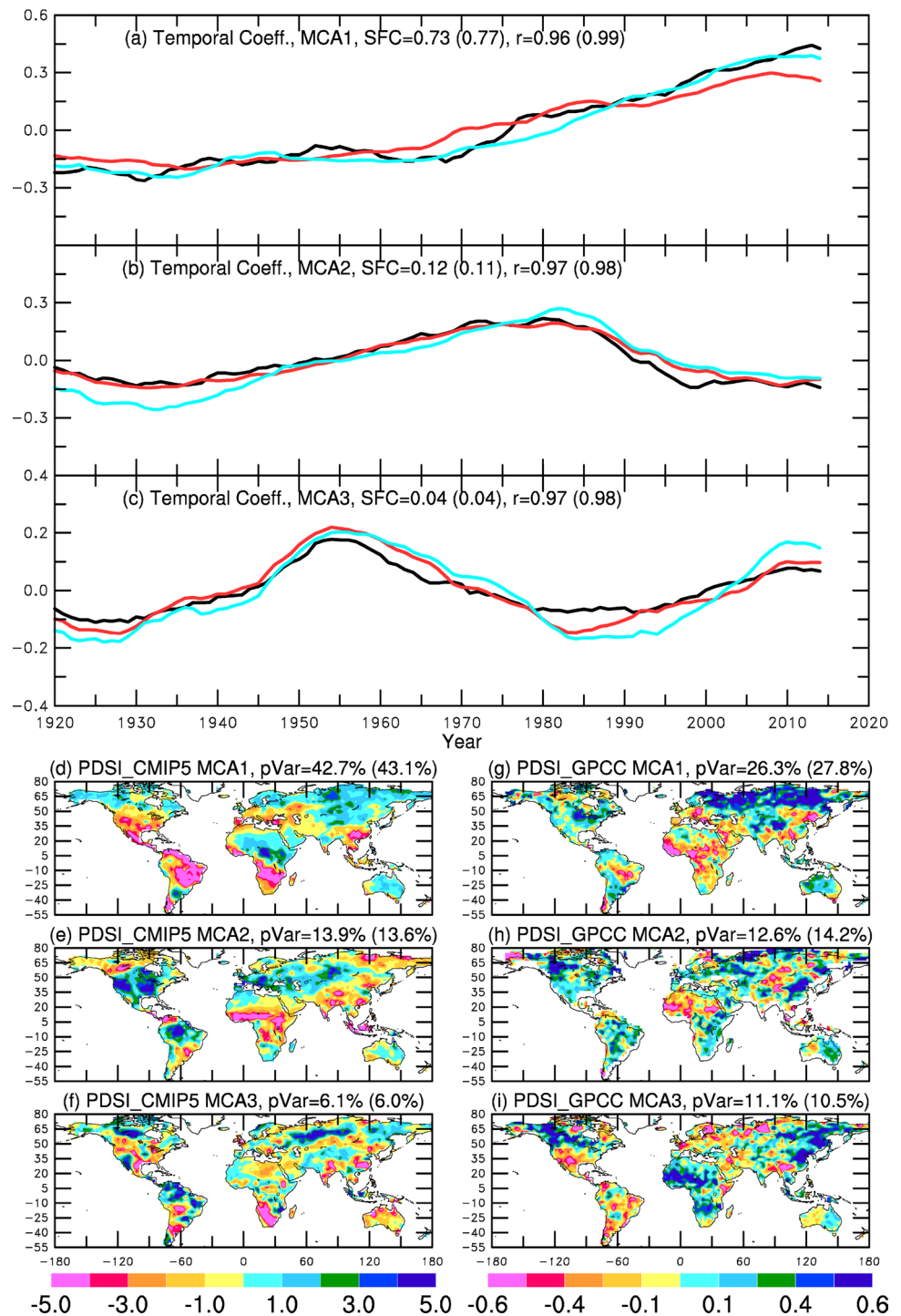
most North America, Southeast South America, and Northwest Australia; but decreased precipitation and runoff over most Africa, eastern Australia, the Mediterranean region, the Middle East, parts of East Asia, central South America, and the Pacific coasts of Canada. The wetting trend over Northwest Australia and Southeast South America is most pronounced in DJF while the drying over Africa and wetting over mid-high latitude Eurasia are seen in all seasons.

These precipitation changes and the drying caused by rising surface temperatures and increasing water vapor deficit have caused surface drying trends and increased risk of drought from 1950 to 2018 over Africa, southern Europe, East Asia, eastern Australia, Northwest Canada, and southern Brazil.

Besides the long-term changes, land precipitation and continental freshwater discharge also show large interannual and inter-decadal variations, with negative anomalies during

El Niño and following major volcanic eruptions in 1963, 1982, and 1991; and their decadal variations are correlated with the IPO with IPO's warm phase associated with below-normal land precipitation and continental discharge. ENSO also dominates the inter-annual variations in scPDSIpm or surface aridity over global land, with wet (dry) conditions during El Niño over Southwest North America, southern South America, and southwestern Asia (northern South America, Australia, South Asia and southern Africa); and the opposite during La Niña. An ENSO-related mode with altered SST patterns and a delayed peak (by ~6 months) also has a significant impact on land aridity. On longer time scales, besides a global trend pattern, the scPDSIpm also shows a multidecadal mode with the period from 1975 to 1998 being relatively dry (wet) over the Sahel, northeastern Asia, Alaska and northern Canada (southwestern North America, most of South America, the Middle East, and most of Europe and Australia); whereas it is the opposite for the periods from about 1945–1974 and since about 1999. This multidecadal mode of land aridity is associated with the multidecadal variability in Pacific and North Atlantic SSTs; together the IPO and AMV account for about 90% of the temporal variations of this mode. Although some of the recent AMV may be externally forced by decadal variations in volcanic and anthropogenic aerosols (Qin et al. 2020a, b), this result still suggests that the IPO and AMV dominate the multidecadal variations in land aridity. While the impact of the IPO and AMV on land precipitation (Dai 2013b; Dong and Dai 2015; Hua et al. 2018) and streamflow (Enfield 2001; Knight et al. 2006) have been examined previously, and the ENSO's impact on land aridity has also been noticed previously (Dai et al. 2004; Dai 2011b; Bonfils et al. 2017; Dai and Zhao 2017), the combined impact by the IPO and AMV on land aridity discussed here is a new finding.

CMIP5 multi-model ensemble mean shows decreased precipitation and runoff and increased aridity and risk of drought during 1950–2018 over Southwest North America, Central America, northern and central South America (including the Amazon), southern and West Africa, the Mediterranean region, and Southeast Asia; while the northern mid-high latitudes, Southeast South America, and Northwest Australia see increased precipitation and runoff. The linear trend patterns and the MCA patterns suggest that the recent wetting (drying) trends from 1950 to 2018 over the northern mid-high latitudes, Northwest Australia, and southeastern South America (southern Europe, Southeast Asia, and West and southern Africa) seen in historical data may be partly forced by external forcing; while the wetting trends over Southwest North America and drying trend over eastern Australia may be mainly related to IPO and other internal variability. Some of the regional trends during 1950–2018 seen in CMIP5 MMM and observations, such as the drying over Southeast Asia (in all seasons) and wetting over Northwest Australia (mainly in DJF and MAM), are absent in the model projections for the 21st century. This suggests that recent volcanic and anthropogenic aerosols and other short-term forcing may have caused these regional changes. Since future emissions scenarios have large uncertainties regarding future volcanic eruptions and other short-term forcing, current model projections of the 21st century hydroclimatic changes may contain large uncertainties over Southeast Asia, Northwest Australia, and other regions that are sensitive to such forcing.

References

Adler RF, Gu G, Sapiano M, Wang JJ, Huffman GJ (2017) Global precipitation: means, variations and trends during the satellite era (1979–2014). Surv Geophys 38:679–699. https://doi.org/10.1007/s10712-017-9416-4

Adler RF, Sapiano M, Huffman GJ, Wang J-J, Gu G, Bolvin D, Chiu L, Schneider U, Becker A, Nelkin E, Xie P, Ferraro R, Shin D-B (2018) The Global Precipitation Climatology Project (GPCP) monthly analysis (new version 2.3) and a review of 2017 global precipitation. Atmosphere 9:138. doi:https://doi.org/10.3390/atmos9040138

Bellomo K, Murphy LN, Cane MA, Clement AC, Polvani LM (2018) Historical forcings as main drivers of the Atlantic multidecadal variability in the CESM large ensemble. Clim Dyn 50:3687–3698

Booth BBB, Dunstone NJ, Halloran PR, Andrews T, Bellouin N (2012) Aerosols implicated as a prime driver of twentieth-century North Atlantic climate variability. Nature 484:228–232. https://doi.org/10.1038/nature10946

Bretherton CS, Smith C, Wallace JM (1992) An intercomparison of methods for finding coupled patterns in climate data. J Clim 5:541–560

Burke EJ, Brown SJ (2008) Evaluating uncertainties in the projection of future drought. J Hydrometeorol 9:292–299

Bonfils C, Co-authors (2017) Competing influences of anthropogenic warming, ENSO, and plant physiology on future terrestrial aridity. J Clim 30:6883–6904

Bonfils CJW, Santer BD, Fyfe JC, Marvel K, Phillips TJ, Zimmerman SR (2020) Human influence on joint changes in temperature, rainfall and continental aridity. Nat Clim Chang 10:726–731. https://doi.org/10.1038/s41558-020-0821-1

Chen M, Xie P, Janowiak JE, Arkin PA (2002) Global land precipitation: a 50-yr monthly analysis based on gauge observations. J Hydrometeorol 3:249–266

Chen J, Dai A, Zhang Y, Rasmussen KL (2020) Changes in the convective potential available energy and convective inhibition under global warming. J Clim 33:2025–2050

Chou C, Neelin JD, Chen C-A, Tu J-Y (2009) Evaluating the "rich-get-richer" mechanism in tropical precipitation change under global warming. J Clim 22:1982–2005

Collins M et al (2013) Long-term climate change: projections, commitments and irreversibility. In: Stocker TF, et al. (ed) Climate change 2013: Thephysical science basis. contribution of working group i to the fifth assessmentreport of the intergovernmental panel on climate change. Cambridge University Press, pp. 1029–1136

Cook BI, Smerdon JE, Seager R, Coats S (2014) Global warming and 21st century drying. Climate Dyn 43:2607–2627

Cook BI, Mankin JS, Marvel K, Williams AP, Smerdon JE, Anchukaitis KJ (2020) Twenty-first century drought projections in the CMIP6 forcing scenarios. Earth's Future 8: e2019EF001461. https://doi.org/10.1029/2019EF001461

Dai A, Fung IY, Del Genio AD (1997) Surface observed global land precipitation variations during 1900–1988. J Climate 10:2943–2962

Dai A (2006) Recent climatology, variability and trends in global surface humidity. J Climate 19:3589–3606

Dai A (2011a) Drought under global warming: A review. WIREs Clim Change 2:45–65

Dai A (2011b) Characteristics and trends in various forms of the Palmer Drought Severity Index during 1900–2008. J Geophys Res 116:D12115

Dai A (2013a) Increasing drought under global warming in observations and models. Nature Climate Change 3:52–58

Dai A (2013b) The influence of the Inter-decadal Pacific Oscillation on U.S. precipitation during 1923–2010. Clim Dyn 41:633–646. DOI https://doi.org/10.1007/s00382-012-1446-5

Dai A (2016) Historical and Future Changes in Streamflow and Continental Runoff: A Review. Chapter 2 of *Terrestrial Water Cycle and Climate Change: Natural and Human-Induced Impacts*, Geophysical Monograph 221, edited by Qiuhong Tang and Taikan Oki, AGU, John Wiley & Sons, pp. 17–37

Dai A, Wigley TML (2000) Global patterns of ENSO-induced precipitation. Geophys Res Lett 27:1283–1286

Dai A, Trenberth KE (2002) Estimates of freshwater discharge from continents: Latitudinal and seasonal variations. J Hydrometeorology 3:660–687

Dai A, Trenberth KE, Qian T (2004) A global data set of Palmer Drought Severity Index for 1870–2002: Relationship with soil moisture and effects of surface warming. J Hydrometeorology 5:1117–1130

Dai A, Qian T, Trenberth KE, Milliman JD (2009) Changes in continental freshwater discharge from 1949–2004. J Climate 22:2773–2791

Dai A, Zhao T (2017) Uncertainties in historical changes and future projections of drought. Part I: Estimates of historical drought changes. Clim Change 144:519–533. DOI:https://doi.org/10.1007/s10584-016-1705-2

Dai A, Zhao T, Chen J (2018) Climate change and drought: A precipitation and evaporation perspective. Current Clim Change Reports 4:301–312. DOI:https://doi.org/10.1007/s40641-018-0101-6

Dai A, Bloecker CE (2019) Impacts of internal variability on temperature and precipitation trends in large ensemble simulations by two climate models. Clim Dyn 52:289–306. https://doi.org/10.1007/s00382-018-4132-4

Deser C, Knutti R, Solomon S, Phillips AS (2012a) Communication of the role of natural variability in future North American climate. Nat Clim Change 2:775–779. https://doi.org/10.1038/nclimate1562

Deser C, Phillips AS, Bourdette V, Teng H (2012b) Uncertainty in climate change projections: the role of internal variability. Clim Dyn 38:527–546

Deser C, Phillips AS, Alexander MA, Smoliak BV (2014) Projecting North American climate over the next 50 years: uncertainty due to internal variability. J Clim 27:2271–2296

Deser C, Terray L, Phillips AS (2016) Forced and internal components of winter air temperature trends over North America during the past 50 years: mechanisms and implications. J Clim 29:2237–2258. https://doi.org/10.1175/JCLI-D-15-0304.1

Döll P, Fiedler K, Zhang J (2009) Global-scale analysis of river flow alterations due to water withdrawals and reservoirs. Hydrol Earth SystSci 13:2413–2432. doi:https://doi.org/10.5194/hess-13-2413-2009

Dong B, Dai A (2015) The influence of the Inter-decadal Pacific Oscillation on temperature and precipitation over the globe. Clim Dyn 45:2667–2681

Dong B, Dai A (2017) The uncertainties and causes of the recent changes in global evapotranspiration from 1982–2010. Clim Dyn 49:279–296. doi:https://doi.org/10.1007/s00382-016-3342-x

Enfield DB, Mestas-Nuñez AM, Trimble PJ (2001) The Atlantic multidecadal oscillation and its relation to rainfall and river flows in the continental U.S. Geophys Res Lett 28:2077–2080

Feng S, Fu Q (2013) Expansion of global dry lands under warming climate. Atmos Chem Phys 13:10081–10094

Fu Q, Feng S (2014) Responses of terrestrial aridity to global warming. J Geophys Res Atmos 119:7863–7875

Fu Q, Lin L, Huang J, Feng S, Gettelman A (2016) Changes in terrestrial aridity for the period 850–2080 from the Community Earth System Model. J Geophys Res Atmos 121:2857–2873. doi:https://doi.org/10.1002/2015JD024075

Gehne M, Hamill TM, Kiladis GN, Trenberth KE (2016) Comparison of global precipitation estimates across a range of temporal and spatial scales. J Clim 29:7773–7795. doi:https://doi.org/10.1175/JCLI-D-15-0618.1

Gu G, Adler RF (2013) Interdecadal variability/long-term changes in global precipitation patterns during the past three decades: Global warming and/or pacific decadal variability? Clim. Dyn 40:3009–3022. doi:https://doi.org/10.1007/s00382-012-1443-8

Gu G, Adler RF (2015) Spatial patterns of global precipitation change and variability during 1901–2010. J Clim 28:4431–4453. doi:https://doi.org/10.1175/JCLI-D-14-00201.1

Harris I, Jones PD, Osborn TJ, Lister DH (2014) Updated high-resolution grids of monthly climatic observations - the CRU TS3.10 Dataset. Intl J Climatology 34:623–642. doi:https://doi.org/10.1002/joc.3711

Hua W, Dai A, Qin M (2018) Contributions of internal variability and external forcing to the recent Pacific decadal variations. Geophys Res Lett 45:7084–7092. https://doi.org/10.1029/2018GL079033

Hua W, Dai A, Zhou L, Qin M, Chen H (2019) An externally-forced decadal rainfall seesaw pattern over the Sahel and southeast Amazon. Geophys Res Lett 46:923–932. https://doi.org/10.1029/2018GL081406

Huang J, Li Y, Fu C, Chen F, Fu Q, Dai A et al (2017) Dryland climate change: Recent progress and challenges. Rev Geophys 55:719–778. DOI:https://doi.org/10.1002/2016RG000550

Huang D, Dai A, Zhu J (2021) Is the subtropical drying a transient response to increased CO_2? J Clim (To be submitted)

Kennedy JJ, Rayner NA, Smith RO, Saunby M, Parker DE (2011) Reassessing biases and other uncertainties in sea-surface temperature observations since 1850. Part 1: measurement and sampling errors. J Geophys Res 116:D14103. doi:https://doi.org/10.1029/2010JD015218

Knight JR, Folland CK, Scaife AA (2006) Climate impacts of the Atlantic Multidecadal Oscillation. Geophys Res Lett 33:L17706. https://doi.org/10.1029/2006GL026242

Knutson TR, Zeng F (2018) Model assessment of observed precipitation trends over land regions: Detectable human influences and possible low bias in model trends. J Climate 31:4617–4637. https://doi.org/10.1175/JCLI-D-17-0672.1

Li X, Zhai G, Gao S, Shen X (2015) Decadal trends of global precipitation in the recent 30 years. Atmos Sci Lett 16:22–26. doi:https://doi.org/10.1002/asl2.514

Liu ZY (2012) Dynamics of interdecadal climate variability: A historical perspective. J Clim 25:1963–1995

Liu C, Allan RP (2013) Observed and simulated precipitation responses in wet and dry regions 1850–2100. Environ Res Lett 8:1–11. doi:https://doi.org/10.1088/1748-9326/8/3/034002

Marvel K, Cook BI, Bonfils CJ, Durack PJ, Smerdon JE, Williams AP (2019) Twentieth-century hydroclimate changes consistent with human influence. Nature 569:59–65

Meehl GA, Stocker TF, Collins WD, Friedlingstein F, Gaye AT et al (2007) Global Climate Projections. *Climate Change 2007: The Physical Science Basis. Contribution of Working Group I to the Fourth Assessment Report of the IPCC*, S. Solomon et al., Eds., Cambridge University Press, pp.746–845

Meinshausen M, Smith SJ, Calvin K et al (2011) The RCP greenhouse gas concentrations and their extensions from 1765 to 2300. Clim Change 109:213. https://doi.org/10.1007/s10584-011-0156-z

Murphy LN, Bellomo K, Cane M, Clement A (2017) The role of historical forcings in simulating the observed Atlantic multidecadal oscillation. Geophys Res Lett 44:2472–2480. https://doi.org/10.1002/2016GL071337

Nguyen P, Thorstensen A, Sorooshian S, Hsu K-L, AghaKouchak A, Ashouri H et al (2018) Global precipitation trends across spatial scales using satellite observations. Bull Am Meteorol Soc 99:689–697

Osborn TJ, Jones PD (2014) The CRUTEM4 land-surface air temperature data set: construction, previous versions and dissemination via Google Earth. Earth System Science Data 6:61–68. DOI:https://doi.org/10.5194/essd-6-61-2014

Palmer WC (1965) Meteorological drought. US Weather Bureau Research Paper 45: 55 pp (Available from https://www.ncdc.noaa.gov/temp-and-precip/drought/docs/palmer.pdf)

Prudhomme C et al (2014) Hydrological droughts in the 21st century, hotspots and uncertainties from a global multimodel ensemble experiment. Proc Natl Acad Sci USA 111(9):3262–3267

Qin M, Hua W, Dai A (2020a) Aerosol-forced multi-decadal variations across all ocean basins in models and observations since 1920. Science Advances 6:eabb0425. https://doi.org/10.1126/sciadv.abb0425

Qin M, Dai A, Hua W (2020b) Quantifying contributions of internal variability and external forcing to Atlantic multidecadal variability since 1870. Geophys Res Lett. https://doi.org/10.1029/2020GL089504

Scheff J, Frierson DMW (2012) Robust future precipitation declines in CMIP5 largely reflect the poleward expansion of model subtropical dry zones. Geophys Res Lett 39:L18704. doi:https://doi.org/10.1029/2012GL052910

Scheff J, Frierson DMW (2014) Scaling Potential Evapotranspiration with Greenhouse Warming. J Climate 27:1539–1558

Schneider U, Becker A, Finger P, Meyer-Christoffer A, Ziese M (2018) GPCC Full Data Monthly Product Version 2018 at 2.5°: Monthly Land-Surface Precipitation from Rain-Gauges built on GTS-based and Historical Data. DOI: 10.5676/DWD_GPCC/FD_M_V2018_250 https://opendata.dwd.de/climate_environment/GPCC/html/download_gate.html

Sheffield J, Wood EF, Roderick ML (2012) Little change in global drought over the past 60 years. Nature 491:435–438. doi:https://doi.org/10.1038/nature11575

Sun Y, Solomon S, Dai A, Portmann R (2007) How often will it rain? J Climate 20:4801–4818

Sun Q, Miao C, Duan Q, Ashouri H, Sorooshian S, Hsu K-L (2018) A review of global precipitation data sets: Data sources, estimation, and intercomparisons. Rev Geophys 56: 79–107. https://doi.org/10.1002/2017RG000574

Taylor KE, Stouffer RJ, Meehl GA (2012) An overview of CMIP5 and the experiment design. Bull Amer Meteorol Soc 93:485–498

Trammell JH, Jiang X, Li L, Liang M, Li M, Zhou J et al (2015) Investigation of precipitation variations over wet and dry areas from observation and model. Adv Meteorol 2015: 1–9. doi:https://doi.org/10.1155/2015/981092

Trenberth KE, Dai A, Rasmussen RM, Parsons DB (2003) The changing character of precipitation. Bull Amer Meteorol Soc 84:1205–1217

Trenberth KE, Smith L, Qian T, Dai A, Fasullo J (2007) Estimates of the global water budget and its annual cycle using observational and model data. J Hydrometeorol 8:758–769

Trenberth KE, Dai A, van der Schrier G, Jones PD, Barichivich J, Briffa KR, Sheffield J (2014) Global warming and changes in drought. Nature Climate Change 4:17–22

van der Schrier G, Jones PD, Briffa KR (2011) The sensitivity of the PDSI to the Thornthwaite and Penman-Monteith parameterizations for potential evapotranspiration. J Geophys Res 116:D03106. doi:https://doi.org/10.1029/2010JD015001

van der Schrier G, Barichivich J, Briffa KR, Jones PD (2013) A scP-DSI-based global data set of dry and wet spells for 1901–2009. J Geophys Res Atmos 118:4025–4048. doi:https://doi.org/10.1002/jgrd.50355

Vicente-Serrano SM, Nieto R, Gimeno L, Azorin-Molina C, Drumond A, El Kenawy A, Dominguez-Castro F, Tomas-Burguera M, Peña-Gallardo M (2018) Recent changes of relative humidity: Regional connections with land and ocean processes. Earth Syst Dyn 9:915–937. https://doi.org/10.5194/esd-9-915-2018

Vicente-Serrano SM, Peña-Gallardo M, Hannaford J, Murphy C, Lorenzo-Lacruz J, Dominguez-Castro F, López-Moreno J, Beguería S, Noguera I, Harrigan S, Vidal J-P (2019) Climate, irrigation, and land-cover change explain streamflow trends in countries bordering the Northeast Atlantic. Geophys Res Lett 46:10821–10833

Vicente-Serrano SM, Quiring S, Peña-Gallardo M, Domínguez-castro F, Yuan S (2020) A review of environmental droughts: Increased risk under global warming? Earth Sci Rev 201:102953. https://doi.org/10.1016/j.earscirev.2019.102953

Willett KM, Berry DI, Bosilovich MG, Simmons AJ (2019) Hydrological cycle: Surface humidity. In *State of the Climate in 2018*. Bull Am Meteorol Soc 100:S25–S27. doi:https://doi.org/10.1175/2019BAMSStateoftheClimate.1

Wang B, Ding Q (2006) Changes in global monsoon precipitation over the past 56 years. Geophys Res Lett 33:L06711. doi:https://doi.org/10.1029/2005GL025347

Wang B, Liu J, Kim H-J, Webster PJ, Yim S-Y (2012) Recent change of the global monsoon precipitation (1979–2008). Climate Dyn 39:1123–1135

Zhang L, Zhou T (2011) An assessment of monsoon precipitation changes during 1901–2001. Climate Dyn 37:279–296

Zhang X, Zwiers FW, Hegerl GC, Lambert FH, Gillett NP, Solomon S, Stott PA, Nozawa T (2007) Detection of human influence on twentieth-century precipitation trends. Nature 448:461–465. doi:https://doi.org/10.1038/nature06025

Zhao T, Dai A (2015) The magnitude and causes of global drought changes in the 21st century under a low-moderate emissions scenario. J Climate 28:4490–4512. doi:https://doi.org/10.1175/JCLI-D-14-00363.1

Zhao T, Dai A (2017) Uncertainties in historical changes and future projections of drought. Part II: Model-simulated historical and future drought changes. Clim Change 144:535–548. DOI https://doi.org/10.1007/s10584-016-1742-x